REPORT DOCUMENTATION PAGE

Form Approved OMB No. 0704-0188

Public reporting burden for this collection of information is estimated to average 1 hour per response, including the time for reviewing instructions, searching existing data sources, gathering and maintaining the data needed, and completing and reviewing the collection of information. Send comments regarding this burden estimate or any other aspect of this collection of information, including suggestions for reducing the burden, to Department of Defense, Washington Headquarters Services, Directorate for Information Operations and Reports (0704-0188), 1215 Jefferson Davis Highway, Suite 1204, Arlington, VA 22202-4302. Respondents should be aware that notwithstanding any other provision of law, no person shall be subject to any penalty for failing to comply with a collection of information if it does not display a currently valid OMB control number.
PLEASE DO NOT RETURN YOUR FORM TO THE ABOVE ADDRESS.

1. REPORT DATE *(DD-MM-YYYY)*
05-01-2005

2. REPORT TYPE
Final Report

3. DATES COVERED *(From – To)*
01-Jun-02 - 15-Feb-05

4. TITLE AND SUBTITLE

Plasma Control of Separated Flows on Bodies of Revolution at High Angles of Attack

5a. CONTRACT NUMBER
ISTC Registration No: 2235p

5b. GRANT NUMBER

5c. PROGRAM ELEMENT NUMBER

6. AUTHOR(S)

Professor Boris Yu. Zanine

5d. PROJECT NUMBER

5d. TASK NUMBER

5e. WORK UNIT NUMBER

7. PERFORMING ORGANIZATION NAME(S) AND ADDRESS(ES)
Institute of Theoretical and Applied Mechanics
Institutskaya st. 4/1
Novosibirsk 630090
Russia

8. PERFORMING ORGANIZATION REPORT NUMBER
N/A

9. SPONSORING/MONITORING AGENCY NAME(S) AND ADDRESS(ES)

EOARD
PSC 802 BOX 14
FPO 09499-0014

10. SPONSOR/MONITOR'S ACRONYM(S)

11. SPONSOR/MONITOR'S REPORT NUMBER(S)
ISTC 01-7036

12. DISTRIBUTION/AVAILABILITY STATEMENT

Approved for public release; distribution is unlimited.

13. SUPPLEMENTARY NOTES

14. ABSTRACT

This report results from a contract tasking Institute of Theoretical and Applied Mechanics as follows: This proposal deals with surface discharge plasmas and other plasma devices to quench stall-slip departure due to 1) asymmetric vortex shedding on conical body nose tips, and 2) augment directional control/authority. In spite of the extensive work in this area, limited understanding of the underlying basic physical processes near body nose tips as they pertain to symmetry-breaking bifurcations still exist. These deficiencies are evident in the scope of previous experimental, theoretical and CFD studies. It is proposed herein to study and assess the impact of using plasmas on the hydrodynamic stability of key flow singular points. The effort will encompass wind tunnel testing, theoretical analysis, development of prediction methods, and evaluation of potential control techniques. It is envisioned that an important spin-off of this effort will be new yaw departure avoidance and control devices based on high-frequency surface discharges. The team of researchers is well positioned to address this problem. Scientists at the Moscow Institute of Physics and Technology (MIPT) have experience in the flow stability and boundary layer separation as well as the combined asymptotics and numerics needed to perform the theoretical and computational investigations of plasma aerodynamics. The Institute of Theoretical and Applied Mechanics in Novosibirsk (ITAM) will perform the wind tunnel testing. ITAM's expertise will add their unique capabilities regarding novel experimental techniques such as: spark discharge excitation procedures and special hot wire methods (weakly invasive and ideally suited to assess the boundary layer separation and vortex structure). In addition, Russian personnel expertise will give fresh insights into the attack on the asymmetric vortex problem and surface discharge mechanisms.

15. SUBJECT TERMS
EOARD, Aviation Technology, Aircraft

16. SECURITY CLASSIFICATION OF:			17. LIMITATION OF ABSTRACT	18, NUMBER OF PAGES	19a. NAME OF RESPONSIBLE PERSON
a. REPORT	b. ABSTRACT	c. THIS PAGE			William B. McClure, Col, USAF
UNCLAS	UNCLAS	UNCLAS	UL	59	19b. TELEPHONE NUMBER *(Include area code)* +44 (0)20 7514 4376

Standard Form 298 (Rev. 8/98)
Prescribed by ANSI Std. Z39-18

ISTC 2235p

Final
Project Technical Report
of ISTC 2235p

Plasma Control of Separated Flows on Bodies of Revolution at High Angles of Attack

(From 1 June 2002 to 30 November 2004 for 30 month)

Boris Yurievich Zanin
(Project Manager)
Institute of Theoretical and Applied Mechanics

Novosibirsk
December 2004

This work was supported financially by European Office of Aerospace Research and Development and performed under the contract to the International Science and Technology Center (ISTC), Moscow.

Contracting Institute: Institute of Theoretical and Applied Mechanics (ITAM) of Siberian Branch (SB) of Russian Academy of Sciences (RAS)
630090, Novosibirsk, Institutskaya St. 4/1, Russian Federation
Phone +7-(383-2) 30-42-79 Fax +7-(383-2) 34-22-68
E-mail: admin@itam.nsc.ru

Participating Institutes: None

Project Manager: Prof. B.Yu. Zanin
630090, Novosibirsk, Institutskaya St. 4/1, Russian Federation
Phone +7-(383-2) 30-42-78 Fax +7-(383-2) 34-22-68
E-mail: zanin@itam.nsc.ru

Project Commencement Date: 1 June 2002
Project Duration: 30 months

Partner: European Office of Aerospace Research and Development
223-231 Old Marylebone Road, London, NW1 5TH, United Kingdom
Phone +44 (0) 20 7514 4953, Fax +44 (0) 20 7514 4960
Email: wayne.donaldson@london.af.mil

Abstract: The objective of this project is the experimental and theoretical research of vortex flow structure control using plasma discharge and other plasma devices to influence on flow separation on conic bodies.

Keywords: subsonic flow, bodies of revolution, boundary layer separation, flow control, electric discharge, smokes visualization.

Contents

List of figures 4
Objective of the project 5
Introduction and overview 5
Expected results 7
Technical approach and methodology 7
Chapter 1. Experimental investigations of flow control by discharge 8
1.1 Technical progress during the first year 8
1.2 Technical progress during the second year 9
1.2.1 Arc discharge 9
1.2.1 Spark discharge 10
1.2.3 Two-channel spark discharge 11
1.3 Technical progress during the final half-year 12
1.3.1 Two-channel spark discharge 12
1.3.2 Barrier discharge 13
Chapter 2. Theoretical and numerical assessment of discharge parameters 13
2.1 Technical progress during the first year 13
2.2 Technical progress during the second year 14
2.2.1 Preliminary assessment of barrier discharge characteristics 14
2.2.2 Statement of problem for modeling the barrier discharge development 17
2.2.3 Results of the calculations 24
2.3 Technical progress during the final half-year 25
Conclusion 29
Perspectives of future developments of researches (for Project prolongation) 29
Attendance to International Conferences 30
Abstracts of published papers 30
References 31
Figures 33-58

List of Figures

Fig. 1.1 Model 1 34
Fig. 1.2 Model 2 34
Fig. 1.3. Scheme of smoke visualization 35
Fig. 1.4 Pressure distribution 35
Fig. 1.5 Visualization, frame 53 36
Fig. 1.6 Visualization, frame 92 36
Fig. 1.7 Visualization, frame 224 37
Fig. 1.8 Electrical circuit of spark discharge 37
Fig. 1.9 Design of model nose section 38
Fig. 1.10 Model assembling 38
Fig. 1.11 Sparking discharge on the model 39
Fig. 1.12 Visualization results at 15 m/s on sharp tip 40
Fig. 1.13 Visualization results at 15 m/s on blunt tip 41
Fig. 1.14 Visualization results at 10,7 m/s on blunt tip 42
Fig. 1.15 Visualization results at 9,2 m/s on blunt tip 43
Fig. 1.16 Nose of model made of a nephritis 44
Fig. 1.17 New spark discharge 44
Fig. 1.18 View of turbulisers and smoke hole 45
Fig. 1.19 Model in test section of wind tunnel 45
Fig. 1.20 Recovery of a symmetry by right discharge 46
Fig. 1.21 Recovery of a symmetry by two discharges 47
Fig. 1.22 Recovery of a symmetry at AOA = 30 dgr. 48
Fig. 1.23 Surface pressure coefficient for right side and both discharges activated 49
Fig. 1.24 Surface pressure coefficient various left discharge voltages 49
Fig. 1.25 Change of vortex configuration with discharge activation 49
Fig. 1.26 Change of vortex configuration for varying discharge power 49
Fig. 1.27 Photo of barrier discharge electrodes 50
Fig. 1.28 Scheme and photo of symmetric barrier discharge on a strap electrode 50
Fig. 1.29 Scheme and photo of asymmetric barrier discharge on a wide upper electrode 51
Fig. 1.30 Scheme and photo of barrier discharge in a gap of wide upper electrode 51
Fig. 2.1 Electrode layout for surface barrier discharge 52
Fig. 2.2 Spatial distribution of specific power deposition 52
Fig. 2.3 Schemes of streamer development in barrier discharge 53
Fig. 2.4 Electron temperature and energy dependence in air 53
Fig. 2.5 Potential distribution in the vicinity of electrode edge 54
Fig. 2.6 Distribution of electric field 54
Fig. 2.7 Dimensionless electron and ion concentration contours 55
Fig. 2.8 Dimensionless electron concentration contours 55
Fig. 2.9 Dimensionless ion concentration contours 56
Fig. 2.10 Surface charge density 56
Fig. 2.11 Spatial distribution of power deposition 57
Fig. 2.12 Power deposition contours 58

Objective of the Project

The objective of this project is the experimental and theoretical research of vortex flow structure control using plasma discharge and other plasma devices to influence on flow separation on conic bodies.

Separation of a flow is one of fundamental problems in the fluid and gas mechanics. In spite of the extensive work in this area, a limited understanding of basic physical processes near body nose tips as they pertain to symmetry-breaking bifurcations still exist. These deficiencies are evident in the scope of previous experimental, theoretical and computational fluid dynamics (CFD) studies. So, it was proposed to study and assess the impact of using plasma on the hydrodynamic stability of key flow singular points. The effort encompasses wind tunnel testing, theoretical analysis, and development of prediction methods and evaluation of potential control techniques. It is envisioned that an important spin-off of this effort will be the new research line of control devices based on high-frequency surface discharges. The team of researchers is well positioned to address this problem and has an experience in the flow stability and boundary layer separation as well as the combined asymptotic and numeric methods needed to perform the theoretical and computational studies of plasma aerodynamics. The Institute of Theoretical and Applied Mechanics in Novosibirsk performs the wind tunnel testing. ITAM's expertise adds its unique capabilities regarding novel experimental techniques such as: spark discharge excitation procedures and special hot wire methods (weakly invasive and ideally suited to assess the boundary layer separation and vortex structure). In addition, Russian personnel expertise gives fresh insights into the attack on the asymmetric vortex problem and surface discharge mechanisms.

Keywords: subsonic flow, bodies of revolution, flow control, boundary layer separation, plasma discharge, smokes visualization.

Introduction and Overview

As repeatedly documented in the literature, (see for example [1]), high angle of attack is critical for vortex structure over flight vehicle forebodies. A key element is freedom from stall and slip departure that can occur because of forebody asymmetric vortex formation. Continuing experience shows that the asymmetric vortex phenomenon can produce forces and moments that are large and evolve rapidly. Both factors may result in an unfavorable flow regime. Conventional solutions to this problem are strakes and slot blowing. Strakes may compromise stealth and blowing may require too much energy to be effective.

Fixed geometry strakes as well as chines could be a point design that might not resolve the stall-spin tendency over the entire flow envelope. Variable and actuated strakes that might be a more global solution however may compromise aerodynamic performance as well as stability and control. They also introduce mechanical complexity and weight issues. MEMS is another possibility, although special micro-fabrication and basic understanding and continuing research is needed to account for the complex issues of this flow in the control laws.

CFD codes have been tried to model these flows. Run conventionally, strong evidence exists that they are inadequate to tackle the special bifurcation, unsteady and non-deterministic aspects of

the vortex dynamics so crucial in understanding the physics. We believe that plasma surface discharges can be effectively used to control this flow. Symmetrical tripping the boundary layer by a simple plasma discharge device may be advantageous compared to the aforementioned schemes due to its simplicity, potential effectiveness and attractiveness for a close-loop feedback system that might include co- and counter- phasing. A potential high impact flip-side opportunity that may have some low-hanging fruit is to use the stall-slip departure tendency for yaw control and tailless capability. This could be one possible outcome of the plasma using.

Although the forebody problem has received much attention [2], important needs must be met before stable and reliable high angle of attack flight can be achieved. One of the difficulties is accurate simulation of the unsteady aerodynamic forces and moments due to the asymmetrical flow pattern. Small local changes of a forebody shape strongly affected aircraft aerodynamic parameters and showed qualitatively new high behaviors.

The importance of the asymmetric vortex phenomenon has prompted much experimental [3]–[14] and theoretical [15]–[20] research. Asymmetrical flow fields arise near the fuselage nose. Downstream from this region, the body shape slightly affects the vortex structure [3]–[5], [7]–[9], [12], [13], [17]–[19]. This feature suggests control of the asymmetry by perturbations close to the nose [3]–[5], [17]–[19] and leads to research on bodies of simple shape, such as a cone and ogive cylinder [3], [4], since such shapes can describe most noses.

Difficulties of simulation of the aerodynamic forces due to asymmetrical vortex structure are caused by:

1. Occurrence of asymmetry is related to absolute rather than convective instabilities of the symmetrical flow field [14], [15]. This leads to strong dependence of the flow pattern on small disturbances, such as vibration of the nose and its roughness [3], [4] and [12], distortion of the nose shape [3], [4], [17]–[19], acoustic noise, and free stream turbulence [3], [7], [8]. CFD computations reveal a strong dependence of vortex structure on truncation errors [17]–[19]. The physics of this instability are not yet understood. The lack of theoretical models thus far has precluded identifying a clear criterion for the origin of instability and development of asymmetry

2. The global vortex structure depends strongly on the location of boundary layer separation. In turn, the location of separation depends on laminar-turbulent transition. However, transition in this connection has not yet been studied. No direct measurements of transition location or its fine structure currently exist. We have only indirect evidence of transition influence on the global vortex pattern such as side force dependence of the aerodynamic forces on the Reynolds number [4] and [9]–[11]. Hunt and Lamont conjecture that «under transitional boundary layer conditions there is no coherent vortex system and the side force becomes very low». This view contrasts to that of Ericsson and Reding who state that «the transitional range is where the maximum side force occurs due to different types of separation on opposite sides». These observations must be interpreted as averages of complicated unsteady processes.

3. Because of Item 2, data obtained in different wind tunnels weakly correlate with each other [3], [21]. Also, they are not easily extrapolated to flight conditions.

To address these issues the proposed project is focuses on fundamental experimental and theoretical studies of the asymmetrical vortex structure for high angle of attack conical bodies and its control using different types of discharges at atmospheric pressure.

Expected Results

The project refers to the category of basic research.

The following results will be obtained under the project implementation:

1. Experimental data on the problem of simulation of high angle of attack conical body aerodynamics accounting for separation and hydrodynamic stability of the vortex structure.

2. Data of theoretical and experimental studies of different kinds of plasma discharges on aerodynamic surfaces and their effect on boundary layer and vortex structures.

3. Data on potential for vortex asymmetry management by active control of the pre-separating boundary layer using aforementioned discharges along the aerodynamic surface.

We believe that a major portion of these results will be useful for understanding of boundary-layer separation phenomenon on bodies of revolution. They will also contribute to fundamental knowledge on the flow disturbance by a discharge to stabilize the vehicle flight at a high angle of attack.

Technical Approach and Methodology

To obtain vortex symmetry over a cone at a high angle of attack we used the analysis of Shalaev *et al* [22]. The main idea therein involved stability of key flow singular points defined from slender body theory as well as boundary layer with volumetric heating considerations, catastrophe and Ginsburg-Landau theories. Out of the work in Ref. [22], a control strategy evolved in which symmetry breaking was avoided by moving the port and starboard cross flow separation points further down the body away from the saddle point in the cross flow plane north pole (toward the equator) using surface discharges. This increases the distance between the vortex cores. It also moves the cross flow saddle point (vortical singularity) closer to the body surface, which is a more stable position to avoid symmetry breaking.

According to estimations [22], the gas heating on 50-100K by a thin cylindrical (around 1mm in diameter) volumetric heat source parallel to the undisturbed separation line is enough to induce the necessary flow separation movement. A lower bound of power deposition has been estimated to be 200 W for a 1 m length cone with power per unit length ~2W/cm.

We used a surface gas discharge as a source of volumetric (as contrasted to surface) heat disturbances in the flow. Such a heat source was created either in a collection of arc or spark breakdowns in short inter-electrode gaps (the total length of the gaps equals 50–70 mm).

The discharge flow control system (DFCS) assumes a set of electrodes implanted flush with the aircraft body surface along the lines of expected flow separation. Depending on freestream characteristics and the angle of attack, different pairs of electrodes can be used to generate a discharge and trip the boundary layer in an appropriate way. DFCS has the following advantages with respect to mechanical or jet system usage for flow perturbation: construction simplicity; massless and inertionless in operation; no changes in aerodynamic shape of the cone; discharge frequency and power variation allow optimal flow disturbances. The proposed discharge application assumes the atmospheric air pressure and subsonic velocities. To generate pressure and temperature disturbances under these conditions we need an energy deposition in relatively narrow regions along boundary-layer separation lines.

For the experimental effort, the low-turbulence T-324 wind tunnel of the Institute of Theoretical and Applied Mechanics of Siberian Branch of Russian Academy of Science (ITAM) was used. Facility parameters are the following: velocity range from 3 to 30 m/s, turbulence intensity, Tu = 0.04%, square test section 1 m 1 m. Experiments performed on a sharp and blunted cones using high-frequency surface discharges. Vortex pictures were obtained by flow visualization based on smoke injection. These were supplemented by surface pressure measurements.

Since unsymmetrical vortex patterns can occur in result of interplay between large-scale global vortex structures and small-scale transition and separation domain of the boundary layer, it is very difficult to develop a rigorous theory of this phenomenon as well as perform direct numerical simulation. However, qualitative analysis does appear to be an effective method for obtaining practical results. The theoretical study was focused on first-order physics models combining experimental data and numerical analysis. These models will be cross-checked by comparisons with the experimental data.

Chapter 1. Experimental investigations of flow control by discharge

1.1. Technical progress during the first year

The following results have been obtained during the first year of the project performance:

- two 5 degree cone models were manufactured;
- experimental equipment to study boundary layer separation on the models has been prepared;
- experimental equipment to create plasma discharge has been manufactured;
- experimental data on vortex patterns on the cone for laminar and turbulent boundary layer separation has been obtained;
- experimental data on a possibility of vortex structure control using arc discharge has been obtained for laminar separation.

Two cone models were manufactured. The length of models is 1 m; the nose half angle is 5 degrees. The model 1 is aluminum made, see Fig. 1.1. The model 2 midsection (Fig. 1.2) is manufactured from caprolon and contains two places for ceramic inserts of 314 mm length and 17 mm width along both sides. The inserts are placed starting 137 mm from the model nose point. Each insert contains a set of flashmounted electrodes; the outer diameter of each one is 4 mm. A gap between pair of the electrodes is from 8 to 10 mm. Thus we are able to generate arc discharges of 8-10 mm length between two electrodes or of 20-24 mm length for three electrodes set engaged. One can change the discharge position at the insert between runs. Some tests have been carried out using the model 2 with blunted nose.

The experiments with cone model were carried out. The conditions of a boundary layer before separation was defined using hot-wire measurements. It was concluded that in a "natural" case, i.e. for the model without turbulizers, the pre-separation boundary layer is laminar for the studied range of angles of attack (AOA) (up to 40 degrees) and flow velocities up to 20 m/s. Visualization of laminar separation on the model surface has been performed.

It was found that if the turbulizing grid was set up at the beginning of a test section, the level of pulsation in a free flow became larger, however in the cone boundary layer pulsation decrease was observed. The turbulent boundary layer before a separation was achieved using two abrasive paper made turbulizers glued on a cone along generatrix. The width of turbulizers is 3 mm, the

height - 1 mm, and the corner between them - 75 degrees. Visualization of turbulent separation on the model surface has been performed.

At the first phase of tests the pairs of small strakes of different profiles and sizes were installed instead of discharge devices. The purpose of experiments was to find zones on the model surface, where flow activation might be most effective. Studies of the vortex configuration above the model were conducted using laser sheet. A single trickle of a smoke was introduced upstream of the model with the laser sheet plane perpendicular to the flow direction. The experiments on the cone model were carried out for bilateral (port and starboard) turbulent boundary layer separation. Turbulent boundary layers before the separation line were obtained using two turbulizers.

The experiments allowed to conclude that vortices above the model without strakes are arranged symmetrically if the AOA is less than 20 degrees for $U_\infty = 20$ m/s. With AOA increasing, the vortex pattern transforms into an asymmetrical one with the direction of asymmetry not being the same for various angles of attack. This is caused by small transient imperfections of the model installation and is an evidence of high sensitivity of the flow to small disturbances.

Possibilities of vortex pattern control were studied for the 25 degrees AOA and $U_\infty = 20$ m/s. Strakes of different length and forms were installed on the model surface to simulate the effect of plasma activators. The purpose of experiments was to determine the best location for the discharge devices to be installed. Our studies showed that it was possible to achieve a symmetrical vortex flow pattern from an asymmetrical initial one. This result can be achieved using two linear strakes very close installed to separation lines of the turbulent boundary layer.
On the next stage of experiments plasma discharges were installed to the position corresponding one of the strakes. The experiments have been performed using arc discharge on the cone model with sharp and blunted nose for the case of laminar flow separation. Blunted configuration was chosen based on following reasons: flow pattern on the sharp configuration is highly sensitive to many parameters, so a repeatability of results is difficult to obtain; our tests have shown that for blunted configuration the arc discharge is more effective. Thus, it is possible to conclude that the discharge effects on an asymmetrical vortex flow above the model. A vortex structure can be switched to symmetrical state using the arc discharge.

1.2 Technical progress during the second year

1.2.1 Arc discharge

New experiments with arc discharge were made for a case of turbulent boundary layer separation. The experiments were performed using a blunted cone model ($R_b = 5$ or 9 mm) in the range of flow velocities 10 to 20 m/sec. Blunted configuration was chosen based on the results of previous tests, to draw the discharges closer to the model nose and raise their efficiency. The surface pressure was measured at ten equidistant stations located in the cross-section x = 576 mm from the cone apex.

The laser knife assisted smoke visualization was performed at the cross-section x =700 mm from the cone apex. Scheme of visualization is shown in Fig. 1.3. The turbulent boundary layer on the model surface was obtained by two turbulizers glued onto the model surface along cone generatrices as described in previous reports. Hot-wire tests were performed to confirm the existence of the turbulence.

The experiments were aimed at revealing the effect of two symmetric arc discharges on flow asymmetry. The electrodes were located 55 mm downstream from the model tip. It should be noted that, owing to some specific features of the electric circuit used, the total discharge power was kept constant, at approximately 120W. This means that, with only one discharge ignited, the power of the discharge was about 120W. After ignition of the second discharge, the power was almost evenly redistributed between the two discharges (about of 60W for each).

The data of Figs. 1.4-1.7 illustrate the effect of symmetric discharges on the vortex pattern of the flow. After the wind tunnel was started up and the undisturbed pressure distribution recorded, smoke injection was performed, followed by application of the high voltage to both electrode pairs. In spite of the fact that both discharge circuits were almost identical, the ignition at the first moment emerged on one pair of electrodes only. Three-five seconds later, the second discharge was ignited. The available range of control was insufficient for a symmetric ignition to be initiated. This non-synchronous ignition was caused by uncontrolled degradation of the electrodes during the experiments.

The experiments were performed for various combinations of flow velocities, angles of attack (AOA), and the model bluntness. Figure 1.4 shows the pressure distributions in a cross-sectional plane of the model at three moments of time: no discharges (video frame #53), only right discharge is active (frame #92), and both discharges are active (frame #224). Figures 1.5, 1.6, and 1.7 show the video frames with streamlines. It can be seen from the figures that the initially symmetric state of the flow was notably distorted by the right discharge and reestablished after the emergence of two symmetric discharges.

1.2.2 Spark discharge

To carry out the experiments with high-frequency linear spark discharges, we used a specially designed electric circuit shown in Fig. 1.8. A pulse from the pulse generator switches the thyratron that provokes the discharge of the capacity C_0, the process being repeatedly reproduced at a frequency defined by the pulse generator. Prior to its discharging, the capacity C_0 had been charged, through a resistor R=41.5 kOm, to a 10-kV voltage by a power source of rectified 50-Hz frequency. The step-up pulse transformers T1 and T2 provided the 20-kV voltage for the capacitors C of two discharge lines. The spark-gap lines were flush-mounted into two sides of the experimental model. The frequency of pulses at the spark gaps was defined by the master frequency of the pulse generator. In preliminary tests, a thyratron with a working frequency up to 400 Hz was used. The discharge lines, each composed by 20 electrodes, were prepared from 0.5-mm diameter cupper wire. The gap between the electrodes was 3 mm and the total length of the discharge lines was 60 mm.

New nose section (Fig. 1.9) was designed and manufactured. To attain sparkling at the model nose surface the electric circuit was made so to support three-gap sparkling at both boards of the model nose. The first electrode was placed 39 mm from the tip, the others spaced in 6 mm interval below. Finally, four electrodes and three 6 mm gaps did the total length of the discharge line of 20 mm. Four capacities were placed in dielectric cases inside the model. The model before final assembling and testing is shown in Fig. 1.10. The tests on a spark discharge ignition on model far from a wind tunnel are conducted (see Fig. 1.11). The electric power input to the discharge line is 20-25 W as thyratron operating frequency was 400 Hz, C_0 charging voltage 4.0-4.4 kV during the experiments.

Wind tunnel experiments were executed for the model with new sparkling discharge device. Narrow range of the flow parameters were chosen as follows: $U\infty = 9.2 \div 15$ m/s, AOA = $17.5 \div 20$ degrees. The goal of the experimental series was to test effectiveness of new plasma actuators and feeding high voltage generator. We concentrated on the discharge application to control the flow in the nose neighborhood for cases of sharp and blunted nose (radius of bluntness 2.5 mm). Experimental data show that the configuration and location of the plasma actuators provide effective vortex wake control for the tested flow parameters. Typical results are presented in the Figs. 1.12-1.15. Plasma channels were about 15 mm long starting from the first electrodes on the both sides of the model. Discharges on both sides of the model were initiated simultaneously or only one (left/right) actuator was used. It was found that initial flow state demonstrate “right asymmetry”, i.e. right vortex core is father from the model than left one. In this case symmetric state could be achieved by activating of the left discharge. At the moment of the plasma appearance the vortex wake switched to symmetric state and remain symmetric until actuators were switched off. Various vortex configurations (asymmetry degree) were obtained depending on flow velocity. The trend is follows: it was possible to obtain clear symmetric vortex wake for $U\infty = 9.2$ m/s, with increasing of U_∞ effect of plasma actuators decreased.

At the end of experiments a strong surface burnout was observed as a result of plasma discharge near the model wall. As a consequence, plasma channel propagated in the burned-out gap beneath the surface and control efficiency decreased. Therefore for next experiments the new nose part made from nephrite was designed and manufactured. It was fireproof.

1.2.3 Two-channel spark discharge

To prevent burnout of the model, the discharge section was made from nephrite see Fig. 1.16), which reduced the possibility of resulting discharge high temperature spikes to the surface. A new hollow second cone section to control capacities inside the model was made. To carry out the experiments with two-channel linear spark discharges, we used the two identical electrical circuits described in the previous paragraph. Discharge lines on both model sides were operated independently in order to adjust the discharge electric power on each of them separately as well as discharge frequency. To accomplish this, two identical power sources were fabricated and a high-voltage impulse scheme was developed. A thyratron with a working frequency up to 1000Hz was used. The discharge lines, each composed of 10 electrodes, were prepared from 0.5mm diameter cupper wire. The gap between the electrodes was 5 mm and the total length of the discharge lines was 50 mm, see Fig. 16. The shining discharge is shown in a Fig. 1.17.

The studies of the flow over the cone model were carried out in the turbulent separation region. The test model had two turbulizers made from abrasive paper, pasted on a cone along generatrices, see Fig. 1.18. All tests were performed for turbulent boundary layer separation conditions. Flow velocity was $U_\infty = 10\text{-}15$ m/s, angle of attack AOA = 15 -30 degrees. For flow visualization, two trickles of smoke were introduced from the orifices on the model surface accompanied by a laser sheet plane perpendicular to the freestream flow. A video camera was installed on the model pylon downstream of the model in this scheme, see Fig. 1.19. These were supplemented by surface pressure measurements.

Experiments were carried out for obtaining detailed recording of the vortex structure behavior versus AOA and determination of the flow pattern dependence on the discharge power.

We concentrated on the discharge application to control the flow in the nose neighborhood for cases of sharp and blunted nose (radius of bluntness is 1 mm). Experimental data show that the configuration and location of the plasma actuators provide effective vortex wake control for the flow parameters studied. Discharges on both sides of the model were initiated simultaneously or only one (left/right) actuator was used. Typical results are presented in the Fig. 1.20. It was found that the initial flow state demonstrated "left asymmetry", *i.e.*, the left vortex core is further from the model than the right one. In this case, a symmetric state could be achieved by activating the right discharge. With increase of discharge power, the vortex wake switched gradually to the symmetric state and remained symmetric until the actuators were extinguished. If the power was further increased, "right asymmetry" was achieved. Various vortex configurations (asymmetry degree) were obtained depending on discharge power. If both discharge lines were activated simultaneously, the flows switched to the symmetric state when a critical level of power was applied, see Fig. 1.21. This value depended on U_∞ and AOA. In our recent tests, the symmetric state of the vortex wake was achieved for AOA's up to 30 degrees, see Fig. 1.22. The asymmetrical picture was in this case obtained at actuation of two discharges and symmetrical at actuation only of right discharge.

1.3 Technical progress during the final half-year

1.3.1 Two-channel spark discharge

Experiments with spark discharge were continued during 9 and 10 quarters. The model configuration was the same as reported in the previous section. The main task of the study was to test high voltage generators with two independent channels. Using this device the power supplied to the right and left spark-gaps can be adjusted independently. At the same time new pressure measurement system was tested. The decision to change pressure measurement system was dictated by high level of electromagnetic radiation produced by spark and barrier discharge. These kinds of discharge were fed by relatively short impulses of high voltage (up to 25 kV on the gap) in contrast to ark discharge, which uses harmonic alternate voltage of industrial frequency. The new system incorporates 'old fashion' multichannel alcohol manometer, video camera and special software for grabbing and digitizing of the image of manometer.

With the two-channel discharge control system, it was possible to control power on each actuator independently and investigate sensitivity of the vortex flow to discharges generated on the left, right and both sides. Figure 1.23 shows the C_p distributions measured in the same cross-section during one run (U_∞ = 10 m/s and α = 22.5°) for the sequence of regimes: both discharges off, right discharge on, both discharges on, both discharges off again. Figure 1.25 shows the associated flow patterns.

This experiment was performed for relatively high angle of attack, with the parameter $\alpha/\varphi = 4.5$. It is well known that for slender bodies of revolution asymmetric vortex flow can be obtained if $\alpha/\theta > 3.5$. In our case the original flow (both discharges off) has *left asymmetry*: a left vortex located higher than the right vortex (Fig. 1.25a). A small misbalance of discharge voltage results in primary ignition of the right discharge. This leads to a sudden change of the vortex asymmetry from the left to the right (Fig. 1.25b) indicating that the separated flow is very sensitive to small perturbations near the nose tip. Further simultaneous increase of voltage of both discharges results in an almost symmetrical vortex arrangement (Fig. 1.25c). This vortex configuration was permanent and stable during the whole period of discharge operation. The vortex flow returned

to the original state with left asymmetry immediately after the discharges were extinguished. An electric power input E = 44.8W for each discharge was used in these experiments.

It can be seen from the C_p distributions in Fig. 1.23 that a change of vortex positions causes significant redistribution of the pressure loads on the model surface. This alteration affects not only the regions near the feeding sheets separation lines but the entire model surface. In addition, it produces appreciable side forces. In several experiments for some combination of U_∞ and α, unstable flutter occurred that caused large model oscillation in spite of a very stiff supporting structure.

For a given direction of vortex asymmetry, the angular pressure distribution consistently responds in a mirror-like fashion giving asymmetry in the opposite direction. As to be expected, symmetric vortex positions give symmetric C_p distributions and no side loads. Small asymmetry of the pressure coefficient that appears as an unsymmetrical distortion of the angular pressure distributions (see Figs. 1.23 and 1.24) may be driven by slight inaccuracy in installation of the turbulizers.

Figures 1.24 and 1.26 show experimental results for In this case, only the left discharge is energized to obtain a symmetric initial state. Since the ratio is close to the critical value of asymmetry occurrence, the side force produced by vortex asymmetry is not too large. Nevertheless, the insights into flow structure can be obtained from these data. It can be seen from the flow visualization that the discharge on the left side of the model significantly changes the vortex positions and the effect is proportional to the voltage applied. Discharge power for these cases was estimated to be 44.8W, 70.2W, and 100.8W. The region of low pressure, corresponding to the left vortex core is shifted away the cone surface as the discharge power increases. This leads to an increase of the surface pressure induced by the vortex on the left side (Fig. 1.24). Pressure changes on the right side are relatively small since the right vortex is weakly affected by the discharge on the left side surface.

1.3.2 Barrier discharge

Experiments with a barrier discharge initiated on a cone surface were carried out. Energy supply was the same as we used in our prior experiments with the discharge. Several electrode geometries were tested for both sharp and blunt (R_b = 2.5 mm) nose configuration. The lower electrode design was the same for all variants. The model body made from dielectric was covered with thin metal foil (copper or aluminum) and was used as lower electrode. Two layers of 0.1 mm lavsan film wrapped the electrode to be an insulator. The second electrodes were glued above it. The frequency varied from 400 to 1000 Hz. Electric power applied to the electrode's gap was up to 120 W. Following configurations were tested:

- Two cupper straps of 3 mm wide placed symmetrically (θ = +/- 90^0). The 280 mm long straps begin 20 mm from the cone tip (see Fig. 1.27).

- One aluminum strap of 2 mm wide placed asymmetrically (θ was varied) and 280 mm in length. It was placed 15 mm apart from the nose tip (see Fig. 1.28).

- One aluminum strap collided partially the lower electrode (see Fig. 1.29). This configuration was tested to obtain the asymmetric barrier discharge. Discharge exists only on the bottom edge of the electrode.

– Two wide aluminum straps connected to each other to obtain the barrier discharge in a gap (see Fig. 1.30).

For all tested configurations the effect of discharge on vortexes position was negligible. Smoke visualization and pressure measurements did not show any significant vortex displacement. In too time the theoretical estimations have shown, that it is possible effectively to effect on flow with the help of barrier discharge. The most probable reason of incongruity of the experimental and theoretical data is insufficient production of heat in the barrier discharge. The additional in-depth experiments in a wind tunnel are indispensable for research of different versions of barrier discharge.

Chapter 2. Theoretical and numerical assessment of discharge parameters

2.1. Technical progress during the first year

During the first year of work on the project we analyzed the applicability of different discharge types for the needed disturbances into flow input. The energy into gas input assessments were carried out for streamer corona, slipping, arc and barrier discharges. The fulfilled investigations have shown the following.

1. For streamer corona and slipping discharge it is difficult to get the necessary volumetric gas heating in a thin filament with fixed spatial location.
2. The arc discharge supplies too high power input, which cannot be governed practically.
3. For all the studied discharge types the surface barrier discharge (SBD) looks the most promising to achieve the goal because of relevant input-power level, stable burning, construction simplicity and the possibility to profile the energy input lane by the electrode curving.

Accordingly, the SBD development in air has been chosen for more detailed numerical investigation for the second year of work at on the project.

Creation of the numerical model for the development of the discharge declared the most perspective on the basis of the first year investigations corresponds to the statement of work and goes according to the schedule.

2.2 Technical progress during the second year

2.2.1 Preliminary assessment of the surface barrier discharge characteristics

The scheme of surface barrier discharge layout is shown in Fig. 2.1. Surface barrier discharge is the repetition in time of the sets of short streamers propagating in the gas along the dielectric surface in the vicinity of the electrode edge nearly perpendicular to the edge. This discharge type is well studied because of its application in ozonators and for gas cleaning from harmful impurities [23]. With the 10 ns accuracy the streamers of each set start almost simultaneously; they are located along the electrode edge at the inter-streamer distance of the order of dielectric thickness.

Streamer development extinction (a streamer set extinction) is due to the streamer transferred charge absorption on the dielectric surface causing the external electric field shielding. If the applied voltage amplitude V_0 is high enough and applied voltage frequency $f << 1/\Delta\tau$, where $\Delta\tau$ = time interval between streamer sets, then a new streamer set arises when the electric field inside the inter-electrode gap reaches again the breakdown value because of applied voltage

increase compensating the shielding action of the surface charge. Accordingly, few sets of streamer breakdown with appropriate current pulses take place on a half period of applied voltage.

According to experimental data, for typical dielectric thickness d = 1-2 mm and relative permittivity $\varepsilon \approx 5$ the current pulse duration τ_{imp} in a single streamer of the surface barrier discharge in atmospheric air is around 50 ns ($\tau_{imp} \approx$ 50 ns), and $\Delta\tau \approx$ 30μs for f = 1 kHz [24].

For SBD presentation by equivalent electrical circuit (Fig. 2.1) the solution for interval $\Delta\tau$ reads [23]

$$\Delta\tau \approx \frac{q_s}{2\pi f C_\varepsilon V_0 \cos 2\pi f t}, \qquad (2.1)$$

where q_s = the total charge transferred by all the streamers of one streamer set, $C_\varepsilon \approx \frac{\varepsilon l l_s}{4\pi d}$ = the dielectric layer capacity, l_s = the streamer length, l = the electrode length along the direction perpendicular to (x, y) plane. Assessment (2.1) coincides with $\Delta\tau \approx$ 30μs by the order of magnitude for characteristic values $q_s/l \approx 10$ nC/cm, $\varepsilon \approx 5$, d = 1-2 mm, $l_s(V_0$=8kV)≈8 mm [24] at f=1kHz. Seeing q_s in air is mainly defined by capacitance of electrode-dielectric system [24], then $\Delta\tau$ practically does not depend on air pressure according to (2.1), i.e. for fixed voltage source parameters the $\Delta\tau$ value could be changed by C_ε value only.

For a case $f << 1/\Delta\tau$ the streamer distribution along the electrode edge is casual without streamer affixment to special points. Accordingly, the dust visualization of SBD in [24] shows the discharge area evenly covers the strip l_s along the electrode edge. The discharge strip width l_s depends on electrode polarity, voltage amplitude and the relative permittivity of the insulator.
The 2-D numerical modeling for a single streamer development in SBD for atmospheric air has been done in [24] for negative electrode polarity V = -11 kV, ε = 5, d = 2 mm. The upper electrode on the dielectric surface was a semicircle with 1 mm radius; it adjoined to dielectric surface by the flat side. The x-axis was directed along the dielectric surface, y-axis was perpendicular to the surface. The reference point was on the electrode edge. The main interesting for us result regarding the magnitude and the spatial distribution of power into air deposition for the time instant corresponding to streamer stop (current pulse extinction) is shown in Fig. 2.2 from paper [24]. These results show that the main energy deposition at the level of $W_e \approx 3$ mJ/cm^3 occurs in the x range from 0.5 to 1.5 mm in the $\delta \approx$ 0.1 mm thickness layer near the insulator surface.

The average power deposition for, for example, f = 1 kHz and $\Delta\tau \approx$ 30μs is

$$W_b = 0.5 W_e/\Delta\tau \approx 50 \text{ W/cm}^3.$$

The 0.5 factor refers to the fact that only one half of the varying voltage time corresponding to the increase of the voltage absolute value is “occupied” by current pulse sets with intervals $\Delta\tau$ between them.
Discharge power P going into air heating along the l =1m length electrode is

$$P = W_b \delta l\, l_s \approx 5 \text{ W},$$

this is 40 times less than the minimal needed value coming from paper [22] assessment.

For discharge power increase it is necessary to increase frequency f ; according to (2.1) this leads to $\Delta\tau$ decrease and average power increase. The maximal power is expected for a case, when there will be only one streamer set for each half a period of applied voltage, i.e. when $f\Delta\tau$ ~ 1. For this case the practical set-up becomes close to the approximation, when the discharge plasma does not decay between the streamer sets and has almost constant electrical conductivity σ, corresponding to streamer plasma conductivity at the end of the current pulse. For this case the solution of equations for equivalent electrical circuit gives the following expressions for potential difference on the discharge gap V_R and discharge power P [25]:

$$V_R = \frac{V_0}{1+\frac{C_p}{C_\varepsilon}} \frac{\omega\tau}{\sqrt{1+\omega^2\tau^2}} \sin(\omega t+\varphi)\,, \qquad (2.2)$$

$$I_R = V_R / R\,, \qquad P = I_R V_R\,, \qquad (2.3)$$

where $C_\varepsilon \approx \frac{\varepsilon l l_s}{4\pi d}$, $C_p \approx \frac{l\delta}{4\pi l_s}$ are the dielectric and the discharge gap capacities, respectively,

$R \approx \frac{l_s}{\sigma\delta l}$ is the discharge gap resistance, ω=2πf, $\tau = R(C_\varepsilon + C_p)$, $\varphi = arctg(\omega\tau)$.

Computations [24] show that for streamer stop time instant in the coordinate x range from 0.5 to 1.5 mm (in the region of power deposition maximum) the electron density $n_e \approx 2\times10^{12}$cm^{-3}, the normal component of electric field E_y=0, the reduced tangential field component E_x/N = 10^{-15} Vcm^2 (N = gas concentration), and the transferred charge density per unit area q_s/ll_s ≈-10 nC/cm^2.

For E/N = 10^{-15} Vcm^2 the average electron energy in air plasma equals 1.9 eV [26], the relevant momentum transfer rate constant for electron-molecule elastic scattering $k_{el} \approx 10^{-7}$cm^3/s [27], and the momentum transfer frequency for atmospheric pressure - $\nu_e = Nk_{el} \approx 2.7\times10^{12}$ s^{-1}.

Plasma conductivity $\sigma = \frac{e^2 n_e}{m\nu_e}$ and σ ≈ 2×10^{-2} Ohm^{-1}m^{-1} = 2×10^8 s^{-1} for aforementioned values of n_e and ν_e. For characteristic values of plasma layer thickness δ ≈0.1 mm, its width l_s ≈ 1mm, electrode length l = 100 cm, insulator thickness d ≈ 1mm and ε = 5

C_p/C_ε <<1, $\tau \approx 2\times10^{-8}$ s, R ≈ 0.5 kOhm.

Accordingly, for f < 100 MHz $\omega\tau$<<1, i.e. the displacement current in the discharge gap is much less than conductivity current, and for average power and current from expressions (2.2), (2.3) follows

$$P = \frac{V_0^2\omega^2\tau^2}{2R}\,, \qquad I_R = \frac{V_0\omega\tau}{R}\sin\omega t\,. \qquad (2.4)$$

For alternative voltage with frequency f = 100 kHz and V_0 = 5 kV (the value, which is close to the bottom boundary of SBD burning) the average power deposition into gas reaches the needed value of P ≈ 250 W, and specific power deposition is

$$W_b = P/(\delta\, l_s\, l) \approx 2500 \text{ W/cm}^3. \qquad (2.5)$$

Further power increase by using much greater than $f \approx 100$ kHz frequencies is difficult because the discharge comes to torch phase and ceases the uniform burning along the electrode edge.

Numerical simulation [24], which results were taken as a basis for power deposition estimation, is still a sole attempt of modeling not a pulse-periodic SBD regime, but a single streamer set. This computation has been fulfilled in the assumption of negative polarity of gas adjacent (top) electrode and the absence of initial dielectric surface charge. The authors have shown that the main physical factor determining air breakdown and near-surface plasma layer formation is the secondary electron emission from the cathode surface.

The obtained results are valid only for a case of the first after the external voltage application current pulse generation. For external voltage polarity changing, when the top electrode becomes an anode, the secondary emission from the cathode covered by dielectric is impossible, and the mechanism of discharge development becomes different. Moreover, the mechanism of discharge development differs from that one proposed in article [24] even for negative polarity of upper electrode in the regime of alternative voltage, because essential role in this case could be played by positive charge on the dielectric surface settled there on the previous stage of discharge development with opposite sign of electrode polarities.

The fact that for the top electrode positive polarity the mechanism of SBD development qualitatively differs from that one proposed in article [24] is confirmed by experiment [28]. It is shown in this work that for a case of dielectrically covered cathode the development of initial electron avalanches is initiated by electron emission from the cathode covering dielectric surface (Fig.2.3b). The number of these electrons is so much, that the ion cloud produced by electron avalanche has a negative charge. As a result, the maximal electric field is formed in the gap between the avalanche cloud and anode, from whence the cathode directed streamer starts.

Remind that the commonly accepted scheme (see Fig. 2.3a), used in particular in [24], assumes the electron avalanches development on the basis of the casual initial electrons and secondary emission electrons from the cathode. According to this scheme the critical for streamer formation charge of the ion cloud inside the inter-electrode gap is achieved due to a set of consequent avalanches; the electrons from these avalanches come away to the anode, and the left slow-moving ions create the positive charge of the ion cloud. The cathode-directed streamer starts from the middle part of inter-electrode gap in this case.

The described schemes for streamer development in volumetric barrier discharge are illustrated in Fig. 2.3 taken from [28].

The schemes of barrier discharge development shown in Fig. 2.3 are valid with some limitations for a case of SBD. The avalanche forming electrons move from cathode to anode. If the top electrode is the cathode, then the distance from the region in the vicinity of the electrode edge, where the avalanches originate, to the dielectric covering the anode is close to zero. Accordingly, the electron avalanches drop the electrons on the dielectric surface much before the critical size of the avalanche is achieved. The cathode-directed streamer is not formed in this case. The discharge development means the motion of dielectric surface charging in the direction out of electrode edge.

In the opposite case the cathode is the electrode covered by dielectric, which emits the electrons. The distances from the top electrode edge (the anode, to which the electrons move) to the outer boundary of the surface discharge region is high enough for avalanches to reach a critical size and create streamer.

The described scenario is confirmed by observations [24]. If the top electrode is a cathode, then the discharge glow near the electrode edge has a diffusive type, the streamers are absent. For a

positive polarity of the top electrode the discharge has a neatly expressed streamer structure with the inter-streamer distance of the order of dielectric thickness.

The width of the streamer zone l_s is few times greater than the diffusive one. Whereas the positive ions land on the dielectric surface in a streamer phase, and the electrons – in a diffusive one, then the surface charge is always positive at a distance from the electrode edge close to the outer boundary of the charged surface region; this also corresponds to experimental data [23, 24].

The foregoing means that SBD development model should necessarily account for the initial (for a time instant of the breakdown threshold achievement) charge distribution on the dielectric surface and the electron desorption from this surface. In this model the absolute value and the spatial distribution of power deposition could significantly differ from the paper [24] predictions not only for the positive polarity of the top electrode, but for the considered in [24] case of negative polarity as well.

2.2.2 Statement of problem for modeling the barrier discharge development in air

2.2.2.1 *Characteristic time and distance scales of the problem*

The stated problem of simulation not just a single streamer set, but a settled SBD burning regime for alternative applied voltage is divided onto two sub-problems with quite different time scales. For promising case of f~100-300 kHz, when only one discharge current pulse develops for each half a period of applied voltage, the time of its formation and proceeding is $\tau_{imp} \approx$ 30-50 ns according to experiment and existing calculations [24], and the time interval between the neighbor current pulses of opposite polarity is $\Delta\tau \sim 1/(2f) \approx$ 2-5 μs. Designate these two discharge stages as A and B stages, or phases, respectively.

Stage A is characterized by electric field at a breakdown level. The breakdown threshold in air is defined by the reduced electric field value $E_{th}/N \approx 1.2\times10^{-15}$ V·cm^2 [25], corresponding to electric field $E_{th} \approx 32.3\times(N/N_0)$ kV/cm, $N_0=2.69\times10^{19}$ cm^{-3}. The characteristic length scale for stage A is the ionization length

$$\lambda_i = \frac{v_{dr}}{k_{ieff} N},$$

and the characteristic time – ionization time

$$\tau_i = \nu_i^{-1} = \frac{1}{k_{ieff} N},$$

where $v_{dr} = K_e E$ is a drift velocity of electron, k_{ieff} is the effective constant of ionization, which equals to the difference of ionization constant and electron attachment to O_2 molecules constant

$$k_{ieff} = k_i - 0.22 k_{att},$$

K_e is a mobility of electrons; the factor 0.22 refers to the relative part of O_2 molecules in air. To estimate the characteristic values of the quantities governing the process of discharge development we choose E/N slightly exceeding the threshold value, when the k_{ieff} becomes positive and reaches the level of its typical values, namely, assume $E_A/N = 1.5\times10^{-15}$ V·cm^2, here E_A is the characteristic value of electric field for stage A

$$E_A = 40.4\times(N/N_0) \text{ kV/cm}.$$

For such a scaling value of reduced electric field the $k_{ieff}(E_A/N)$ = 2.09×10^{-11} cm^3/s, the drift velocity $v_{dr}(E_A/N)$ = 1.5×10^{7}cm/s [29], and the length and time of ionization

$$\lambda_i(E_A/N) = 0.027\frac{N_0}{N}\text{ cm}, \qquad \tau_i(E_A/N) = 1.78\cdot 10^{-9}\left(\frac{N_0}{N}\right)\text{s}. \tag{2.6}$$

The rest of characteristic parameters is convenient to obtain by means of using the dimensionless variables in the main equations describing the considered problem, namely, the Poisson equation for electric field

$$\nabla\cdot\mathbf{E} = 4\pi e(n_i - n_- - n_e) \tag{2.7}$$

and electron transport equation

$$\frac{\partial n_e}{\partial t} + div\left(-D_e\nabla n_e - n_e K_e\mathbf{E}\right) = S\,. \tag{2.8}$$

Here n_i, n_- are the concentrations of positive and negative ions, K_e, D_e = mobility and diffusion coefficient for electrons, S = the total source of electron arising and deceasing, in particular, $S = k_{ieff}n_e N$ for the processes of ionization by electron impact and binary attachment.

Use the dimensionless coordinates, time and electric field by relations

$$t' = \frac{t}{\tau_i}, \quad r' = \frac{r}{\lambda_i}, \quad E' = \frac{E}{E_A}\ .$$

The Poisson equation reads

$$\nabla'\cdot\mathbf{E}' = n_i' - n_-' - n_e', \tag{2.9}$$

where $n_i' = \frac{n_i}{n_0}$, $n_-' = \frac{n_-}{n_0}$, $n_e' = \frac{n_e}{n_0}$ are the dimensionless concentrations of ions end electrons normalized by

$$n_0 = \frac{E_A}{4\pi e\lambda_i}; \tag{2.10}$$

n_0 appears as a factor in the right side of equation (2.7) as a result of using the dimensionless variables.

It should be emphasized that n_0 is not a characteristic electron density value for stage A, because n_e grows up by orders of magnitude in the process of avalanche evolution, but n_0 is a measure for charged particles density, which is necessary to create the electric field of the order of E_A by charge separation at the λ_i distance scale. Accordingly, n_0 is of the order of magnitude of charged particles density at the final leg of stage A, when the charge separation induced electric field is around E_A and streamer develops. For E_A = 40.4×(N/N_0) kV/cm

$$n_0 = 0.82\times 10^{12}\left(N/N_0\right)^2\text{ cm}^{-3}. \tag{2.11}$$

This order of magnitude for electron density in SBD plasma for a time instant of current pulse extinction (stage A extinction) is confirmed by calculations [24].

The electron transport equation after using the dimensionless variables and Einstein relation for K_e and D_e

$$D_e = \frac{K_e T_e}{e} \tag{2.12}$$

reads

$$\frac{\partial n'_e}{\partial t'} + \nabla' \cdot (-n'_e \mathbf{E}' - \Pi_1 \nabla' n'_e) = n'_e \frac{k_{ieff}(E/N)}{k_{ieff}(E_A/N)},$$

where $\Pi_1 = \frac{k_B T_e}{e E_A \lambda_i}$ is a dimensionless parameter, which is equal to the ratio of electron average energy to the energy electrons get from the electric field on the distance λ_i, or the ratio of electron diffusion flow to the drift flow, k_B = Boltzmann's constant.

In order to define the characteristic time and length scales for stage B similar to (2.6) and to concretize the ion composition of plasma for both stages, we have to analyze the proceeding kinetic processes.

2.2.2.2 Ion composition of plasma

a) *Positive ions*

During the electron avalanche development and for streamer propagation stage the ions N_2^+, O_2^+ are produced due to ionization by electron impact. The rate constants for N_2 and O_2 ionization are defined by *E/N* value and calculated using electron energy distribution function resulting from the Boltzmann's equation solution [29]; these data were approximated by the dependencies [30]

$$k_{iN_2} = 10^{-8.09 - \frac{40.29}{\gamma}} \text{ cm}^3/\text{s}, \quad k_{iO_2} = 10^{-8.31 - \frac{28.57}{\gamma}} \text{ cm}^3/\text{s}, \qquad 8 < \gamma < 30, \tag{2.13}$$

$$k_i = 0.78 k_{iN_2} + 0.22 k_{iO_2} = 10^{-7.95 - \frac{38.22}{\gamma}} \text{ cm}^3/\text{s}, \tag{2.14}$$

where $\gamma = E/N$ value in units of 10^{-16} V·cm^2.

As a result of a chain of conversion and charge transfer reactions the ions N_2^+, O_2^+ convert into ions O_2^+ and O_4^+. The conversion time $\tau_c \sim 1\times(N_0/N)$ns, and it is much less than $\tau_{imp} \sim 30$ ns for atmospheric pressure, so the main types of positive ions are ions O_2^+, O_4^+ for all the stages of discharge plasma evolution.

The equilibrium concentrations of these ions are approximately equal to each other according to fulfilled estimates used the rate constants from [31]. The time of equilibrium settling in the chain of direct and reverse reactions

$$O_2^+ \leftrightarrow O_2^+ N_2 \rightarrow O_4^+ \leftrightarrow O_2^+$$

is around 10 ns for atmospheric pressure and effective temperature of ion-molecular collisions T_{ieff} = 500K, $T_{ieff} = (m_i T_i + m_a T)/(m_i + m_a)$, where m_i, m_a are the masses of colliding ion and molecule. The ion and gas temperature difference is defined by relation [32]

$$T_i - T = \frac{m_i + m_a}{3k_B}(K_i E)^2 . \qquad (2.15)$$

More detailed information regarding O_2^+ and O_4^+ ion concentration ratio is redundant for our problem, because the mobility of these ions differs only by 20%, that is inside the accuracy limits for determination of their concentrations, and their dissociative recombination with electrons can be neglected comparing to recombination with negative ions. The latter has an equal rate for O_2^+ and O_4^+ ions in contrast to dissociative recombination.

b) *Negative ions*

For air plasma the negative ions are produced as a result of two reactions of electron attachment to O_2 molecules: the dissociative reaction with energetic threshold

$$e + O_2 \rightarrow O^- + O, \qquad k_{att} = 10^{-10.21 - \frac{5.7}{\gamma}} \text{ cm}^3\text{/s [30]}, \qquad (2.16)$$

and three-body reaction without threshold

$$e + 2O_2 \rightarrow O_2^- + O_2, \quad \alpha_{att} = 4.45 \times 10^{-31} \text{ cm}^6\text{/s [31]}.$$

If $\gamma > 5$ ($E/N > 5\times10^{-16}$ V·cm^2), the dissociative attachment (2.16) is dominant for atmospheric pressure. For less pressure this predominance is extended to smaller values of reduced electric field. For a considered case of sinusoidal applied voltage, when for stage A the characteristic electric field greater than its breakdown value ($E_A/N = 15\times10^{-16}$ V·cm^2), the expected electric field values for stage B, except the time instant of external voltage polarity changing, have to be greater than γ=5 despite the external field shielding by the surface charge. This assumption is confirmed by calculations [24], showing that the electric field at the end of SBD current pulse is slightly less than the breakdown value - $E/N \approx 10^{-15}$ V·cm^2, $\gamma \approx 10$. Thus, for air pressures not greater than atmospheric the main negative ion in SBD plasma is O^- ion produced in dissociative attachment (2.16).

The characteristic attachment time is

$$\tau_{att} \approx (7 \div 40) \times \left(\frac{N_0}{N}\right) \text{ns for } \gamma = 15 \div 5 \quad . \qquad (2.17)$$

Analysis of different channels of ions O^- disappearance shows that for considered conditions the main processes are: theelectron detachment in collisions with N_2

$$O^- + N_2 \rightarrow e + N_2O, \qquad k_{dt}(\gamma = 10) = 9.2 \times 10^{-13} \text{ cm}^3\text{/s [33]}, \qquad (2.18)$$

and the recombination with positive ions

$$O^- + A^+ + M \rightarrow O + A + M, \quad M = N_2, O_2, \; A^+ = O_2^+, O_4^+, \qquad (2.19)$$

for air densities $N > 0.4N_0$ the reaction (2.19) rate ceases its dependence on density N_M and its rate constant reaches the binary process value

$$k_r = 2\times10^{-6}\left(\frac{300}{T_i(K)}\right)^{1.5} \text{ cm}^3\text{/s [34]}. \qquad (2.20)$$

The characteristic electron detachment time $\tau_{dt} \approx 40\left(\frac{N_0}{N}\right)$ns and the characteristic recombination (2.19) time for expected according to (2.11) maximal charged particles density $n_i \sim n_0 \sim 10^{12}$ cm^{-3} is $\tau_r \approx 0.5$ μs. Accordingly,

$$\tau_{imp} \approx \tau_{dt} << \Delta\tau \text{ and } \tau_{imp} << \tau_r < \Delta\tau,$$

this means both ion-ion recombination and electron detachment should be accounted for stage B, and only detachment - for stage A; moreover, in the first approximation the detachment could be neglected at stage A, like it was done in equation (2.9), because $\tau_{dt} \approx \tau_{imp}$.

The competitor of ion-ion recombination is the electron-ion dissociative recombination:

$$e + O_2^+ \rightarrow O + O, \qquad k_{dr1} = 2\times10^{-7}\left(\frac{300}{T_e(K)}\right)^{0.7} \text{ cm}^3\text{/s [31]},$$

$$e + O_4^+ \rightarrow O_2 + O_2, \qquad k_{dr2} = 1.4\times10^{-6}\left(\frac{300}{T_e(K)}\right)^{0.5} \text{ cm}^3\text{/s [31]}.$$

Electron temperature T_e is defined by reduced electric field. According to calculation [29] $T_e \approx$ 2.7 ÷ 3.3 eV for γ = 10÷15. For expected according to (2.11) $n_e \sim n_0 \sim 10^{12}$ cm^{-3} and γ ≈ 10÷15 the characteristic times of ions O_2^+ and O_4^+ dissociative recombination $\tau_{dr1} \approx$ 150μs >> $\Delta\tau$ and $\tau_{dr2} \approx$ 8μs > $\Delta\tau$, respectively; they greater than not only the attachment time (2.17) and ion-ion recombination time $\tau_r \approx$0.5μs, but the time interval between the current pulses. Accordingly, the dissociative recombination can be neglected for all the staged of discharge evolution, if the electron concentration does not rise to 10^{14}cm^{-3} value.

Thus, electron impact ionization, dissociative attachment (2.16) and, possibly, the detachment (2.18) should be accounted for stage A. For stage B the accounted for processes are electron attachment (2.16) and detachment (2.18) plus the ion-ion recombination (2.19).

Seeing $\tau_{att} \sim \tau_{dt} << \tau_r$ the electrons and negative ions are in equilibrium in phase B, and the characteristic time of the problem is $\tau_r \approx$0.5μs. The characteristic length is the thickness of plasma layer δ≈0.01 cm [24] produced at the stage A. Comparing these values with the characteristic length and time (2.6) for stage A, note than the characteristic lengths are of the same order of magnitude, but the times differ approximately 200 times. These features are accounted for numerical solution.

2.2.2.3 Transport coefficients

The diffusion coefficient and mobility for positive and negative ions obey the Einstein relation (2.12) with appropriate ion temperature calculated by formula (2.15). From literature data [26] the mobility of O_2^+, O_4^+ ions in nitrogen at normal conditions are $K_{O_2^+} = 2.4$, $K_{O_4^+} = 2.05$, and for ion O^- in oxygen [35] - $K_{O^-} = 3.2$ in units cm^{2}V^{-1}s^{-1}. Because of close molecular masses of O_2, N_2 and from the known data for another ions these values could be accepted equal to the

mobilities of these ions in air. In our calculations we assume for positive and negative ions respectively

$$K_i = 2.1\times\left(\frac{N_0}{N}\right)\left(\frac{300}{T_i(K)}\right)^{0.3}\ \text{cm}^2\text{V}^{-1}\text{s}^{-1}, \quad K_ = 3.2\times\left(\frac{N_0}{N}\right)\left(\frac{300}{T_(K)}\right)^{0.3}\ \text{cm}^2\text{V}^{-1}\text{s}^{-1}. \quad (2.21)$$

The temperature dependencies are taken from the book [35]. The diffusion coefficients corresponding to these mobilities are D_i = 0.054, D_- = 0.083 cm^2/s at normal conditions.

For electrons in external electric field K_e and D_e are the functions of reduced electric field E/N (or γ) and, generally speaking, do not obey the relation (2.12). Thereby the magnitude of characteristic electron energy is defined as

$$T_{ch} = \frac{eD_e}{K_e}\ , \quad (2.22)$$

following from the Einstein relation (2.12), depending on E/N and being the analog of the temperature in equilibrium medium. The approximation of calculation [29] data reads

$$k_B T_{ch} = 1.61 + 0.11\gamma\ \text{eV},\ \text{for}\ 8 < \gamma < 30\ , \quad (2.23)$$

$$K_e = 0.6\times10^3\left(\frac{N_0}{N}\right)\ \text{cm}^2\text{V}^{-1}\text{s}^{-1}\ \text{for}\ \gamma < 8\ , \quad (2.24)$$

$$K_e = 0.37\times10^3\left(\frac{N_0}{N}\right)\ \text{cm}^2\text{V}^{-1}\text{s}^{-1}\ \text{for}\ 8 < \gamma < 30\ . \quad (2.25)$$

The relations (2.22) – (2.25) determine K_e and D_e in SBD plasma. The non-answered question remains how T_{ch} refers to average electron energy

$$T_e = \frac{2}{3k_B}\int_0^\infty \varepsilon f(\varepsilon) d\varepsilon\ , \quad (2.26)$$

which is used in the rate constants of some kinetic processes with electron participation? Function $f(\varepsilon)$ in (2.26) is the electron energy distribution function normalized by unity.

We did not find the answer on this question in literature and made our own numerical calculation of electron energy distribution function in air similar to [29] on the basis of previously developed code [36]. The results for T_{ch} and T_e are shown in Fig. 2.4. For $\gamma > 10$ the difference between T_{ch} and T_e is small, but for $\gamma < 10$ it becomes notable and should be accounted for.

2.2.2.4 *System of equations*

The coordinate system and the region of SBD simulation is shown in Fig. 2.1. We consider 2-D development of the discharge in (x,y) plane, assuming its uniform distribution along the top electrode edge flush mounted with the dielectric surface. The applied voltage frequency f~100 kHz corresponds to the case of maximal power deposition into gas, when only one streamer set takes place on each half a period of applied voltage.

Aforecited analysis has shown that the following system of equations is relevant for our problem solution

$$\frac{\partial n_i}{\partial t} + div\mathbf{J}_i = k_i N n_e - k_r n_e n_i + S_{ph}, \quad \mathbf{J}_i = -D_i \nabla n_i + n_i K_i \mathbf{E}, \tag{2.27}$$

$$\frac{\partial n_-}{\partial t} + div\mathbf{J}_- = 0.22 k_{at} N n_e - k_{dt} n_- N, \qquad \mathbf{J}_- = -D_- \nabla n_- - n_- K_- \mathbf{E}, \tag{2.28}$$

$$\frac{\partial n_e}{\partial t} + div\mathbf{J}_e = k_i N n_e - k_r n_e n_i - 0.22 k_{at} N n_e + k_{dt} n_- N + S_{ph}, \quad \mathbf{J}_e = -D_e \nabla n_e - n_e K_e \mathbf{E}, \tag{2.29}$$

$$\mathbf{E} = -\nabla \varphi \tag{2.30}$$

$$\Delta\varphi = -4\pi e(n_i - n_- - n_e) \qquad \text{for gas region } (y>0), \tag{2.31}$$

$$\Delta\varphi = 0 \qquad \text{for dielectric region } (-d<y<0). \tag{2.32}$$

The conditions for gas-dielectric boundary for y=0, x>0

$$\left.\frac{\partial\varphi}{\partial x}\right|_{0+} = \left.\frac{\partial\varphi}{\partial x}\right|_{0-}, \tag{2.33}$$

$$\left.\frac{\partial\varphi}{\partial y}\right|_{0+} = \varepsilon \left.\frac{\partial\varphi}{\partial y}\right|_{0-} - 4\pi\sigma(x,t), \tag{2.34}$$

where σ is the surface charge density

$$\sigma(x,t) = e\int_0^t (J_{iy} - J_{-y} - J_{ey})dt, \qquad \sigma(x, t=0) = 0. \tag{2.35}$$

Boundary conditions for electric potential are

φ =0 for y=-d,

$$\varphi = V_0 \sin 2\pi f t \quad \text{for } y=0,\ x<0, \tag{2.36}$$

$$\varphi = V_0 \sin(2\pi f t) \times \left[\frac{1}{2} - \frac{1}{\pi} arctg\left(\frac{x}{y}\right)\right] \quad \text{for } y \to \infty,\ x \to \pm\infty. \tag{2.37}$$

The condition (2.37) arises from asymptotic solution of equation $\Delta\varphi = 0$ in semi-plane with boundary conditions (2.36).

The boundary conditions for charged particles concentrations are

$$n_i = n_e = n_{in}, \quad n_- = 0, \qquad \text{for } y \to \infty \text{ and } y=0,\ x \to \pm\infty, \tag{2.38}$$

$$J_{ey} = -K_e n_e E_y - D_e \frac{\partial n_e}{\partial y} = \sigma_e \nu_e^{des} - n_e V_{eT} \qquad \text{for } y=0,\ x>0, \tag{2.39}$$

$$n_i = n_- = n_e = 0 \quad \text{for } y=0,\ x<0. \tag{2.40}$$

The condition (2.40) on the electrode surface is a condition of particle flow absence from the surface. It is designedly correct for ions of both sign, but for electrons it should be substituted by the condition of the electron secondary emission from electrode surface, if the top electrode is the cathode

$$J_{ey} = -\gamma_s J_{iy}, \tag{2.41}$$

where γ_s is a secondary emission coefficient.

The condition (2.39) is the definition of hydrodynamic flow of electrons by the kinetic flow in the near-surface layer on gas-dielectric boundary. Here σ_e = the surface density of electrons, ν_e^{des} = the frequency of electron desorption from the dielectric surface, $V_{eT} = \sqrt{\frac{2k_B T_e}{\pi m_e}}$ is the thermal velocity of electrons.

The σ_e is determined by solution of equations

$$\frac{\partial \sigma_e}{\partial t} = -\sigma_e \nu_e^{des} + n_e V_{eT} - \alpha_{rw} \sigma_e \sigma_+ , \tag{2.42}$$

$$\frac{\partial \sigma_+}{\partial t} = -J_{iy} - \alpha_{rw} \sigma_e \sigma_+ , \tag{2.43}$$

where σ_+ is the surface density of positive ions, α_{rw} = the coefficient of electron-ion recombination on the surface.

According to paper [37] results $\nu_e^{des} \approx 5\times10^3$ s^{-1}, a $\alpha_{rw} \approx 10^{-7}$cm^{2}s^{-1}.

The initial conditions are

$$n_i = n_e = n_{in}, \quad n_- = 0, \quad \sigma(x,0) = 0 \quad \text{for } t=0. \tag{2.44}$$

The source S_{ph} describes the gas photo ionization by UV radiation from the discharge area, which is necessary for streamer development. This effect is modeled by accepted procedure, when S_{ph} = 0 is assumed, and the background electron density n_{in} ~10^8 cm^{-3} is postulated.

In the transport equations the kinetic and transport coefficients are the functions of local reduced field. Because of comparability of electric field non-uniformity length and λ_i the non-local effects should be accounted for. The investigation of this effect in [38] has shown that it really notably changes the value of n_e and electric field distribution in the head of streamer, but induces small changes of the current inside the streamer channel and power deposition. Our objective is to calculate the power into gas deposition; accordingly, the local field approximation is valid.

2.2.3 Results of calculations

For numerical solution of 2-D non-stationary system of equations for ions and electrons transport with Poisson equation for electric field potential the numerical code has been created realizing the variable directions technique.

On the first phase of calculations the initial spatial electric field distribution has been obtained. The results for potential and the absolute value of electric field are shown in Fig. 2.5 and 2.6 for unity value of potential difference between the electrodes.

For the positive polarity of the top electrode the barrier discharge comes into experimentally observed streamer phase, if the ionization Townsend coefficient $\alpha = \lambda_i^{-1}$ not only positive, but high enough inside the region at some l_x distance from the electrode edge. Namely, the following condition should be carried out [25]

$$\int_{x_0}^{l_x} \alpha(x)dx \geq 20 \cdot$$

In calculated initial spatial distribution of electric field this condition is valid for $(l_x - x_0)/d \approx 1.1 - 1.2$ (x_0 is the coordinate of electrode edge) and potential difference 5-6 kV; this agrees with experimentally observed threshold of barrier discharge burning in atmospheric air for dielectric thickness d=1mm.

The self-consistent computation of electrodynamics and kinetics did not succeed yet to get a reliable result for discharge dynamics. We pursue the code testing to reveal the bags in numerical algorithm and its realization. When this work will be finished the objective will be achieved; we will get the magnitude and the spatial distribution for SBD power input into gas in the regime of periodically varying applied voltage.

2.3 Technical progress during the final half-year

The performed analysis has shown that the system of equations describing the stage of barrier discharge development corresponding to electrical current pulse flowing through the gas (phase A) can be reduced to the following non-dimensional equations

$$\frac{\partial n'_e}{\partial t'} - \nabla' \cdot (n'_e \mathbf{E}'_e) = n'_e \frac{k_{ieff}(E/N)}{k_{ieff}(E_A/N)}, \tag{2.51}$$

$$\frac{\partial n'_i}{\partial t'} = n'_e \frac{k_i(E/N)}{k_{ieff}(E_A/N)}, \tag{2.52}$$

$$\frac{\partial n'_-}{\partial t'} = n'_e \frac{0.22 k_{att}(E/N)}{k_{ieff}(E_A/N)}, \tag{2.53}$$

$$\Delta\varphi' = -(n'_i - n'_e - n'_-), \tag{2.54}$$

$$E' = -\nabla'\varphi'. \tag{2.55}$$

where $t' = \frac{t}{\tau_i}$, $r' = \frac{r}{\lambda_i}$, $E' = \frac{E}{E_A}$ – the dimensionless time, coordinate, electric field, and $n'_i = \frac{n_i}{n_0}$, $n'_- = \frac{n_-}{n_0}$, $n'_e = \frac{n_e}{n_0}$ – the dimensionless ion and electron concentrations, normalized by

$$n_0 = \frac{E_A}{4\pi e \lambda_i}, \qquad n_0 = 0.82 \times 10^{12} \left(N/N_0\right)^2 \text{ cm}^{-3}. \tag{2.56}$$

The characteristic electric field value for phase A is

$$E_A = 40.4 \times (N/N_0) \text{ kV/cm}, \tag{2.57}$$

ionization length

$$\lambda_i(E_A/N) = 0.027 \frac{N_0}{N} \text{ cm}, \tag{2.58}$$

and ionization time

$$\tau_i = \nu_i^{-1} = \frac{1}{k_{ieff} N}, \qquad \tau_i(E_A / N) = 1.78 \cdot 10^{-9} \left(\frac{N_0}{N} \right) \text{s}. \tag{2.59}$$

Effective ionization rate constant k_{ieff} equals to the difference between ionization rate constant k_i and dissociative electron attachment to O_2 molecules rate constant k_{att}; $k_{ieff} = k_i - 0.22 k_{att}$, N = air density, $N_0 = 2.69 \times 10^{19}$ cm^{-3}.

Boundary and initial conditions for Eqs.(2.51)-(2.55) have been discussed and described in previous section.

The main task of the last two quarters of the work on the project was the solution of Eqs.(2.51)-(2.55) to obtain the deposited power into gas spatial distribution.

All the attempts to solve the problem by standard gridding approaches like splitting and variable-direction techniques failed because of numerical instability development. To avoid this, Particle-in-Cell (PIC) technique was finally applied for transport equations (2.51)-(2.53) solution. Poisson equation for electric potential is still solved by upper relaxation technique (the improved Ziedel technique).

The PIC technique can be used for discharge phase A description because of negligible electron and ion diffusion comparing to their drift. In the first approximation it is also possible to neglect the ion drift for characteristic phase A time ($\tau_{imp} \approx 30$ns). The PIC technique usage made it possible to overcome the numerical difficulties in self-consistent solution of Eqs.(2.51)-(2.55) and to realize the discharge development modeling.

The first test for the obtained solution was a comparison of calculated and experimentally observed breakdown (threshold) voltage V_{th} for negative polarity of upper electrode.

The discharge development is assumed to start when the condition

$$\int_{C_{th}} \frac{dl}{\lambda_i(E)} \geq 1 \text{ , where } \lambda_i(E) = \frac{v_{dr}(E)}{k_{ieff}(E) N}, \tag{2.60}$$

becomes valid for some E-field strength line C_{th} from the electrode surface to the surface of dielectric. After $\lambda_i(E)$ expression substitution into non-equality (2.10) it transforms to

$$\int_{C_{th}} 10 \frac{N}{N_0} \exp\left(\frac{7.89\kappa}{1+\kappa} \right) \frac{1 - \exp\left(-\frac{6.71\kappa}{1+\kappa} \right)}{1+\kappa} dl \geq 1, \tag{2.61}$$

$$\kappa = \frac{E(x,y) - E_{th}}{E_{th}}, \quad E_{th} = 11.14 \cdot 10^{-16} N \text{ V/cm}.$$

The strength line C_{th} is that one, on which the integral in expression (2.60) achieves its maximum value. Calculations show that this line starts practically from the electrode edge (starting point $x_0 \approx -0.1$ mm) and that integral in expression (2.60) overcomes unit value for electrode voltage $V = -4.15$ kV on strength line C_{th} crossing the dielectric surface at $x_C = 1.35$ mm. This line length is $l_C = 2$ mm and maximum y-coordinate value is $y_C = 0.33$ mm. The region $0 < x < x_c$, $0 < y < y_c$ near the electrode edge is a starting region for discharge development.

These results correspond to the experimental data and validate the accuracy of electric field calculation with no volume charge for considered electrode system.

The numerical modeling of discharge plasma evolution lead us to the conclusion, that the assumed physical model for barrier discharge development is not correct and can not describe this phenomenon. The initially present in the volume electrons are swept by electric field to the dielectric surface without their sufficient breeding, so the discharge ceases before the electron concentration reaches notable value needed for air glowing. The results of calculation for V = -4.9 kV, dielectric permittivity ε = 10, dielectric thickness d = 1 mm are shown in Fig. 2.7 for dimensionless electron and ion concentration contours. For the time instant $t \approx 50$ ns all the electrons are near the dielectric surface far away from electrode edge. The electron concentration in the region with high electric field value (near the electrode edge) equals to zero. The maximum n_e is around $0.003n_0$ and corresponding gas heating is negligible comparing to experimental data.

To improve the model, the air ionization by UV photons emitted by discharge region should be accounted for. This process seems to be a key mechanism for barrier discharge development, because it may create new electron-ion pairs in the region of high electric field, which, in turn, gives rise to new electron avalanches. Accordingly, the transport equations for electrons and ions have been modified to read

$$\frac{\partial n'_e}{\partial t'} - \nabla' \cdot (n'_e \mathbf{E}'_e) = n'_e \frac{k_{ieff}(E/N)}{k_{ieff}(E_A/N)} + S_{ph}, \tag{2.62}$$

$$\frac{\partial n'_i}{\partial t'} = n'_e \frac{k_i(E/N)}{k_{ieff}(E_A/N)} + S_{ph}, \tag{2.63}$$

where

$$S_{ph} = \beta_{ph} \frac{n'_e(x'_m, y'_m)\exp(-1/E'(x'_m, y'_m))}{1 + (x' - x'_m)^2 + (y' - y'_m)^2} \tag{2.64}$$

is an approximation for non-dimensional photoionization source; $x'_m(t'), y'_m(t')$ – are the coordinates of the point with maximum electron concentration for current time instant, β_{ph} – is a scaling parameter. By trial and error technique we choose β_{ph} = 0.1 in our calculations.

The results of barrier discharge evolution modeling accounting for the photoionization effect are shown in Figs. 2.8-2.12 for V = - 4.9 kV, ε = 10, d = 1 mm. The electrode edge coordinates are x = 0 and y = 0.

With accounted for air photoionization the calculated electron concentration inside the discharge cloud raises up to the values of the order of n_0 as shown in Fig.2.8. This thin cloud with a width approximately equal to 0.05 – 0.1 mm propagates along the dielectric surface on the distance around 3 mm during the time ~ 50 ns.

The ion cloud practically does not change its position and ion concentration number during the time interval from 8 to 50 ns (see Fig.2.9). Accordingly, all the electron breeding starts and occurs near the electrode edge. The created electron cloud drifts in electric field toward dielectric surface without notable increase of electron concentration on this way.

The electrons reaching the dielectric surface form a surface charge in the adsorption-desorption process. The calculated surface charge distribution along the dielectric surface for different time instants is shown in Fig.2.10. To obtain the surface charge absolute values these data should be multiplied by $\sigma_{e0} = en_0\lambda_i$ = 3.5 nC/cm^2.

The main objective of our numerical investigation – the spatial distribution of discharge power input into the gas for different time instants is shown in Fig.2.11. Figure 2.12 presents the data for the time instant t = 53.4 ns in a larger scale. To obtain absolute values of power deposition these data should be multiplied by factor $w_0 = en_0 v_{dr0} E_A$ =7.95×10^4 W/cm^3.

The obtained results for power deposition coincide on the order of magnitude with the numerical results obtained by other authors, our preliminary estimations and assessments done from experimental data. The discharge breakdown voltage and discharge zone length are close to those observed in the experiment.

The developed numerical model for barrier discharge evolution contains an unknown parameter "governing" the air photoionization process due to radiation from the discharge region. To obtain more rigorous results additional both numerical and experimental investigations are needed to clarify the description of photoionization source and another stages of discharge development.

Conclusion

Investigations presented in this report have shown that vortex symmetry breaking above a cone at angle attack can be avoided by means of surface discharge activators. In our application of this concept, discharges were distributed along the conical generatrices near the cone nose tip. Both symmetric and asymmetric activation were tested to understand and quantify the control laws.

Experiments on a sharp cone model revealed difficulties in the application of actuators located relatively far downstream from the model nose. A key result of our investigation is verification of the surface discharge plasma symmetry-breaking control concept with nose blunting.

The results obtained show that arc and spark electric discharges can be effectively used to control vortex asymmetry on forebodes in subsonic flows. Changing the power of electric discharges and switching between different electrodes can control positions of the vortex cores and model side force. Furthermore, it is possible to obtain a desired asymmetry, (say for tailless control), or eliminate it by applying appropriate discharge power. Thus, besides avoidance of symmetry breaking our work shows that side force can be smoothly controlled with spark discharges placed near separation lines feeding the cross flow vortices.

The developed numerical model for barrier discharge evolution contains an unknown parameter. To obtain more rigorous results additional both numerical and experimental investigations are needed to clarify the description of photoionization source and another stages of discharge development.

Experiments with a barrier discharge initiated on a cone surface were carried out. For all tested configurations the effect of discharge on vortexes position was negligible. The additional in-depth experiments in a wind tunnel and theoretical investigations are indispensable for research of different versions of barrier discharge.

Perspectives or future developments of researches (for Project prolongation)

Our experiments clearly demonstrated robustness of the plasma discharge for symmetry breaking control. However the limited understanding of the underlying basic physical processes leading to symmetry breaking still exist. Important spin-off of this effort is the new theoretical concept, which has been elaborated by Malmuth et al. [22, 39]. According to this concept the vortex asymmetry is due to instability of the saddle point occurring between two concentrated vortices at supercritical angles of attack. The saddle point occurrence, in turn, depends on locations of the boundary-layer separation lines. By manipulating the separation lines it is feasible to control stability of the saddle point and the vortex symmetry breaking. The saddle-point criterion [39] predicts the critical angles of attack, which agree with available experimental data and our observations. However, direct measurements of the saddle point and the separation lines have not been performed and the theoretical predictions [22,39] have not been verified by experiments. Detailed and well-documented data on the vortex flow structure and its coupling with the boundary-layer separation are also needed for verification of other theoretical models and CFD studies. Toward filling of this gap, the proposed effort will be focused on systematic experimental investigations of the vortex-structure characteristics (vortex trajectories, saddle point occurrence etc.) and their correlation with boundary-layer separation induced by various forcing. The major outcome of this effort will be a comprehensive database, which in combination with the theoretical modeling [22,39] will provide a good launching pad for design of new control devices based on high-frequency surface discharges.

The in-depth experiments on analysis of effect of barrier discharge on vortex asymmetry will be conducted. The necessity of such experiments is called by outcomes of the theoretical investigations described in the given report and shown that it is possible effectively to effect on flow with the help of barrier discharge. The different versions of barrier discharge will be investigated and the comparison of the experimental and theoretical data will be conducted.

This effort will be closely coordinated with the theoretical effort of Dr. Malmuth (Rockwell Scientific Company, California). This symbiosis makes our program team to be well positioned to address the problem. The ITAM adds unique capabilities regarding novel experimental techniques such as its spark discharge excitation procedures and special hot wire methods that it are ideally suited to assess the boundary-layer separation and hydrodynamic stability features to be studied in the proposed effort.

Attendance to International Conferences

1). There were the business trip of Prof. A.A. Maslov and Prof. B.Yu. Zanin on 42nd AIAA Aerospace Sciences Meeting (Reno, Nevada, January 5-8, 2004) for presentation of results of researches under the given project. The business trip is paid at the expense of EOARD. Title of presentation:
A.A. Maslov, B.Yu. Zanin, A.A. Sidorenko, V.P. Fomichev, A.A. Pavlov, B.V. Postnikov, N. Malmuth. Plasma control of separated flow asymmetry on a cone at high angles of attack.

2). The results of investigations were presented on International Conference on the Methods of Aerophysical Research (Novosibirsk, Russia, June 28 – July 03, 2004). Title of presentation:
A. Maslov, B. Yu. Zanin, A. A. Sidorenko, V. P. Fomichev, A. A. Pavlov, B. V. Postnikov, N. Malmuth Conical bodies flow control by plasma discharge.

Abstract of published papers

A.A. Maslov, B.Yu. Zanin, A.A. Sidorenko, V.P. Fomichev, A.A. Pavlov, B.V. Postnikov, N. Malmuth. Plasma control of separated flow asymmetry on a cone at high angles of attack *AIAAPaper 2004-843*. – 42 AIAA Sciences Meeting and Exhibit, 5-8 January 2004, Reno, Nevada – 8 pp.

A. A. Maslov, B. Yu. Zanin, A. A. Sidorenko, V. P. Fomichev, A. A. Pavlov, B. V. Postnikov, N. Malmuth Conical bodies flow control by plasma discharge *Proc. Int. Conference on the Methods of Aerophysical Research.* - Novosibirsk, 2004. - Part. 1 - p. 164-169.

V.M. Fomin, A.A. Maslov, B.Yu. Zanin, A.A. Sidorenko, V.P. Fomichev, B.V. Postnikov, and N. Malmuth “Electric-Discharge Control over a Vortex Flow around Bodies of Revolution”. *Doklady Physics*, 2004, v.49, No. 6.

These papers deals with surface discharge plasmas and other plasma devices to control or eliminate vortex symmetry breaking on conical forebodies at incidence. Control of separated flows is one of fundamental problems in fluid mechanics. An important example is high angle attack forebody flows. In spite of extensive effort, limited understanding of the underlying basic physical processes near body nose tips as they pertain to symmetry-breaking bifurcations still exist. These deficiencies are evident in previous experimental, theoretical and CFD studies. These papers discuss a new surface discharge scheme that shows promise in controlling

symmetry breaking. Results of wind tunnel experiments that we have conducted are discussed. The work to be described herein focuses on experimental studies of influence of different types of discharge on asymmetric vortex structures at atmospheric pressure levels, typical of forebody high angle of attack flows.

References

1. Skow, A.M., and Peake, D.J., «AGARD Lecture Series No. 121, «High Angle of Attack Aerodynamics,» AGARD-LS-121, pp. 10-1–10-22, March 1982.
2. AGARD Lecture Series No. 121, «High Angle of Attack Aerodynamics,» AGARD-LS-121, March 1982.
3. Hunt, B.L., «Asymmetric Vortex Forces and Wakes on Slender Bodies,»AIAA Paper No. 82-1336, 1982.
4. Ericsson, L.E., and Reding, J.P., «Aerodynamic Effects of Asymmetric Vortex Shedding from Slender Bodies,» AIAA Paper No. 85-1797, 1985.
5. Keener, E.R., Chapman, G.T., Cohen, L., and Telegani, J., «Side Forces on Forebodies at High Angles of Attack and Mach Numbers of 0.1 to 0.7: Two Tangent Ogive, Paraboloid and Cone,» NASA TM X-3438, 1977.
6. Keener, E.R., «Oil Flow Separation Patterns on an Ogive Forebody,» AIAA J., 21, No. 4, pp. 550–556, 1983.
7. Lamont, P.J., and Hunt, B.L., «Pressure and Force Distributions on a Sharp-Nosed Circular Cylinder at Large Angles of Inclination to an Uniform Subsonic Stream,» J. Fluid Mech., 76, No. 3, pp. 519–529, 1976.
8. Dexter, P.C., «A Study of Asymmetric Flow over Slender Bodies at High Angles of Attack in Low Turbulence Environment,» AIAA Paper No. 84-0505, 1984.
9. Lamont, P.J., «Pressure around an Inclined Ogive Cylinder with Laminar, Transitional, or Turbulent Separation,» AIAA J. , 20, No. 11, pp. 1492 - 1499, 1982.
10. Lamont, P.J., «The Effect of Reynolds Number on Normal and Side Forces on Ogive Cylinder at High Incidence,»AIAA Paper No. 85-1799, 1985.
11. Champigny, P., «Influence du nombre de Reynolds sur les caracteristiques aerodynamics d'une configuration ogive-cylindre a grand incidence,» a Recherche Aerospatiale, No. 6, pp. 417 - 425, 1984.
12. Moskovitz, C.A., Hall, R.M., and De Jarnette, F.R., «Effects on of Nose Bluntness, Roughness and Surface Perturbations on the Asymmetric Flow past Slender Bodies at Large Angles of Attack,» AIAA Paper No. 89-2236, 1989.
13. Ziliac, G.G., Degani, D., and Tobak, M., «Asymmetric Vortices on a Slender Body of Revolution,» AIAA J,. 29, No. 5, pp. 667–675, 1991.
14. Lowson, M.V., and Ponton, A.J.C., «Symmetric Breaking in Vortex Flows on Conical Bodies,» AIAA J. 30, No. 6, pp. 1576 - 1583, 1992.
15. Tobak, M., and Peake, D.J., «Topology of Three-Dimensional Separated Flows,» Annual Review of Fluid Mechanics 14, pp. 61 - 85, 1982.
16. Fiddes, S.P., «Separated Flow about Cones at Incidence–Theory and Experiments,» Studies of Vortex Dominated Flows, Springer Verlag, NY, pp. 185–310, 1987.
17. Hartwich, P., Hall, R., and Hemsch, M., «Navier-Stokes Computations of Vortex Asymmetries Controlled by Small Surface Imperfections,» AIAA Paper No. 90-0385, 1990.
18. Degani, D., «Numerical Investigation of the Origin of Vortex Asymmetry,» AIAA Paper No. 90-0593, 1990.
19. Siclari, M.J., «Asymmetric Separated Flows at Supersonic Speeds,» AIAA Paper No. 90-0595, 1990.
20. Poll, D.I.A.,»Some Effects of Boundary Layer Transition on Slender Axisymmetric Bodies at Incidence at Incompressible Flow,» AGARD Symp. on Missile Aerodynamics, Tronheim, Norway, Paper 13, 1982.
21. Champigny, P.G., «Stability of Side Forces on Bodies at High Angles of Attack,» AIAA 4–th Applied Aerodynamic Conference, pp. 72–78, 1986.
22. Shalaev V., Fedorov A., Malmuth N. et al, *AIAA Paper* 2003-0034, Reno, NV (2003)

23. Samoylovich V.G., Gibalov V.I., Kozlov K.V., Fizicheskaia khimiia bar'ernogo razriada (Physical chemistry of barrier discharge), M., Izdatelstvo Moskovskogo Universiteta, 1989.
24. Gibalov V.I., Pietsch G.J., *J. Phys. D: Appl. Phys*., V.33, 2618-2636 (2000)
25. Raizer, Yu.P., Gas Discharge Physics, Springer, Berlin, 1991.
26. Physicheskie velichiny, Handbook edited by I.S. Grigoriev, E.Z.Meilikhov, M., Energoatomizdat, 1991, P. 430.
27. Eletskii A.V., Palkina L.A., Smirnov B.M., Iavleniia perenosa v slaboionizovannoi plasme, M., Energoatomizdat, 1975, P.185.
28. Kozlov K.V., Wagner H-E., Brandenburg R., Michel P., *J. Phys. D: Appl. Phys*., V.34, 3164-3176 (2001).
29. Aleksandrov N.L., Visikailo F.I., Islamov R.Sh., Kochetov I.V., Napartovich A.P., Pevgov V.G., *High Temp*., V. 19, №1, 22-27 (1981).
30. Aleksandrov N.L., Bazelyan A.E., Bazelyan E.M., Kochetov I.V., *Sov.Plasma Phys.*,**21**, 60 (1995).
31. Kossyi I.A., Kostinsky A.Yu., Matveyev A.A., Silakov V.P., *Plasma Sources Sci. Technol*., V.1, 207-220 (1992).
32. Wannier, G.H., *Bell. Syst. Techn. J.*, V.32, No.1, 170 (1963).
33. Aleksandrov N.L., Bazelyan E.M., Kochetov I.V., Dyatko N.A., *J.Phys.D: Appl. Phys.*, V. 30, 1616-1624 (1997).
34. Smirnov B.M., Negative ions, New York: McGraw-Hill, 1982.
35. Smirnov B.M., Ioni i vozbuzhdennie atomi v plasme, M., Atomizdat,1974.
36. Aleksandrov N.L., Konchakov A.M., Son E.E., *Sov.Plasma Phys.*, V.4, No.5, P.1182 (1978).
37. Golubovskii Yu.B., Maiorov V.A., Behnke J., Behnke J.F., *J. Phys. D: Appl. Phys*., V.35, 751-761 (2002).
38. Naidis G.V., *Pis'ma v ZHTF*, V.23, № 12, 89-93 (1997).
39. Shalaev V., Fedorov A., Malmuth N., and Shalaev I., "Mechanism of Forebody Nose Symmetry Breaking Relevant to Plasma Flow Control," *AIAA Paper 2004-842*, 2004.

The Figures

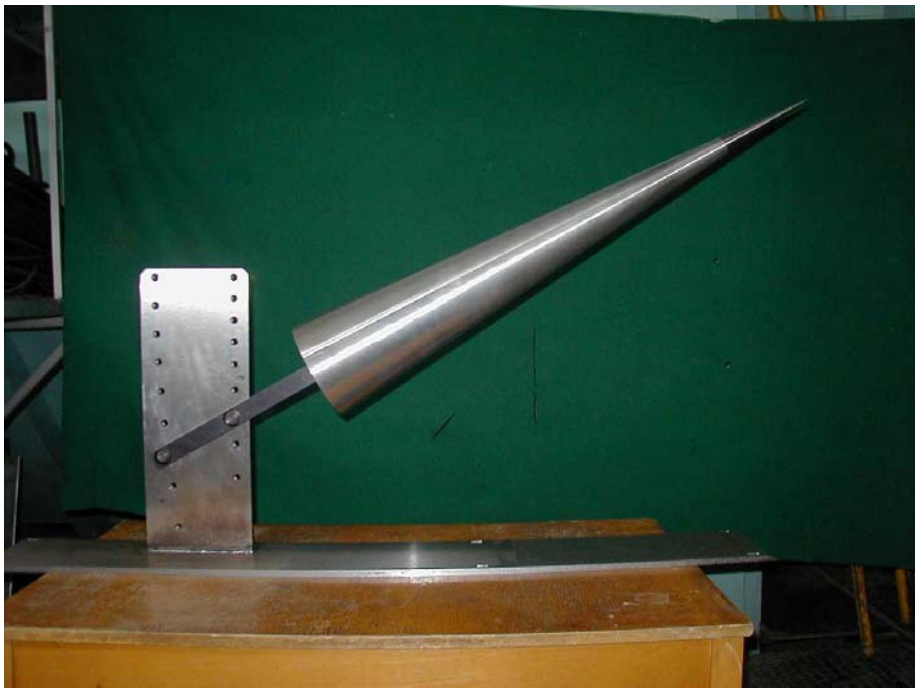

Fig. 1.1. Model 1

Fig. 1.2. Model 2

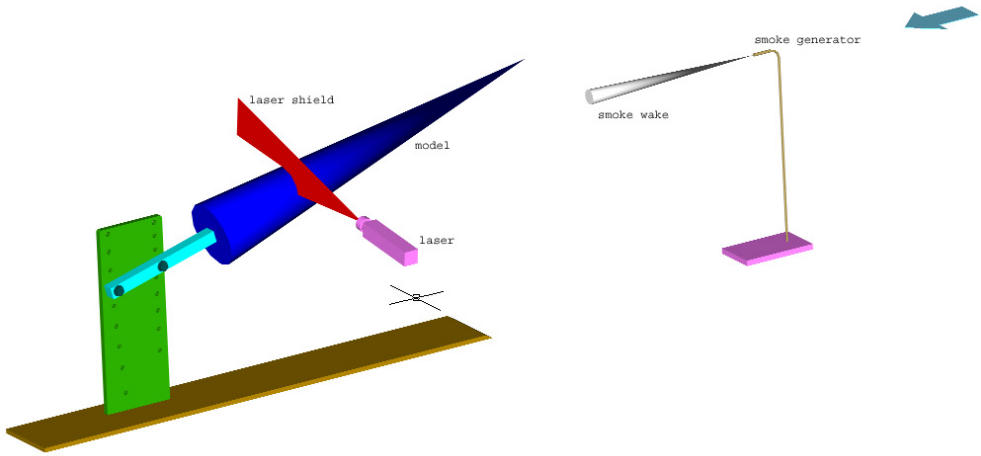

Fig. 1.3. The scheme of smoke visualization

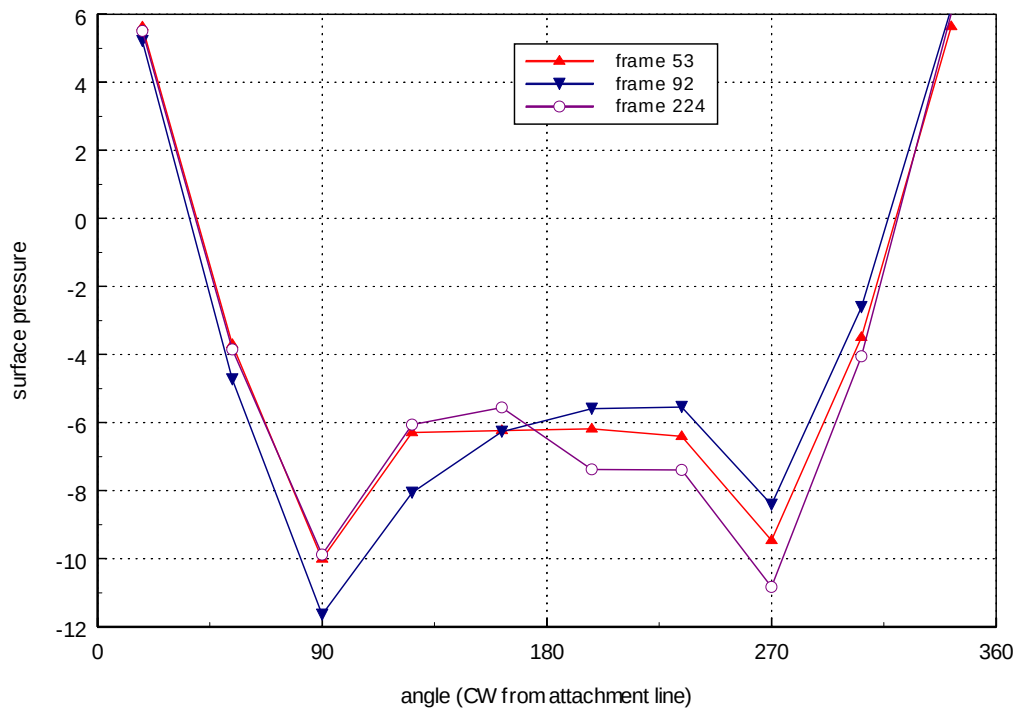

Fig. 1.4. Pressure distribution corresponded to three different discharge states. AOA=20 deg., U = 15 m/s

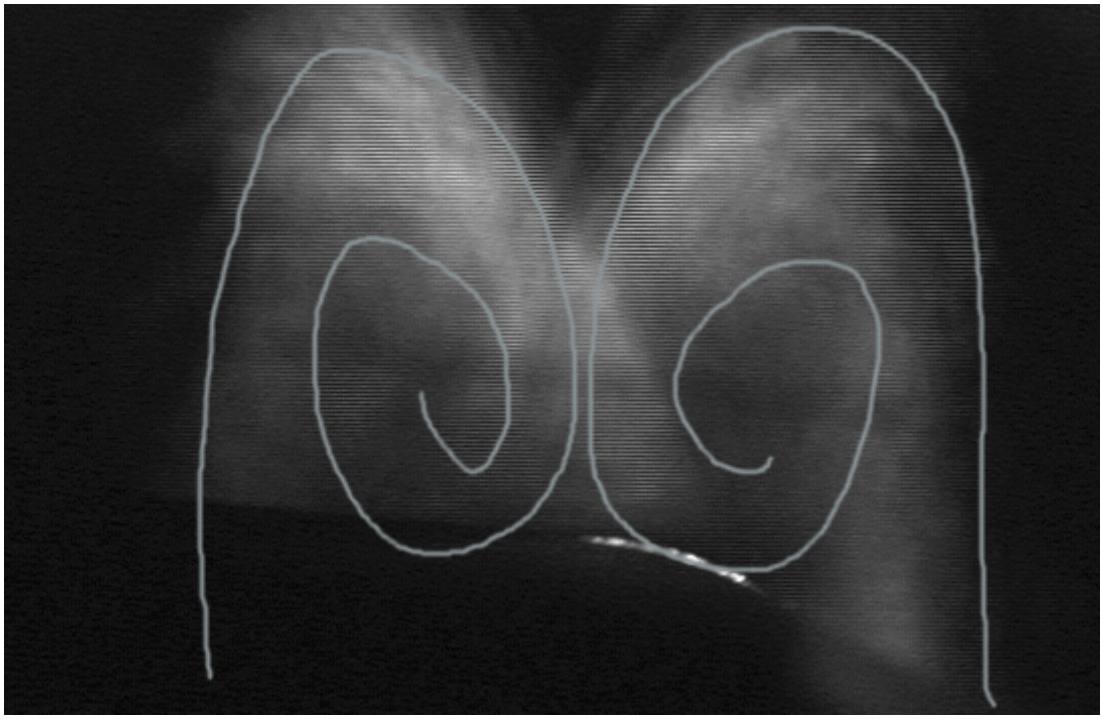

Fig. 1.5. Laser knife flow visualization, frame 53. (gray lines show streamline projections on the vertical plane)

Fig. 1.6. Laser knife flow visualization, frame 92. (gray lines show streamline projections on the vertical plane)

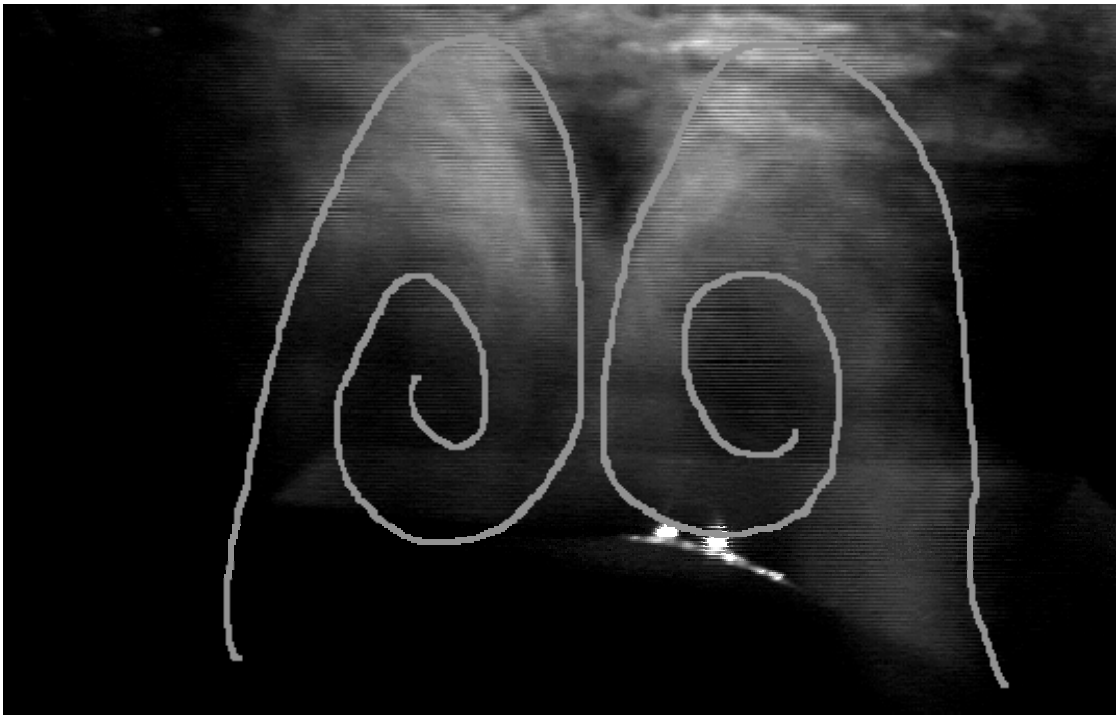

Fig. 1.7. Laser knife flow visualization, frame 224. (gray lines show streamline projections on the vertical plane)

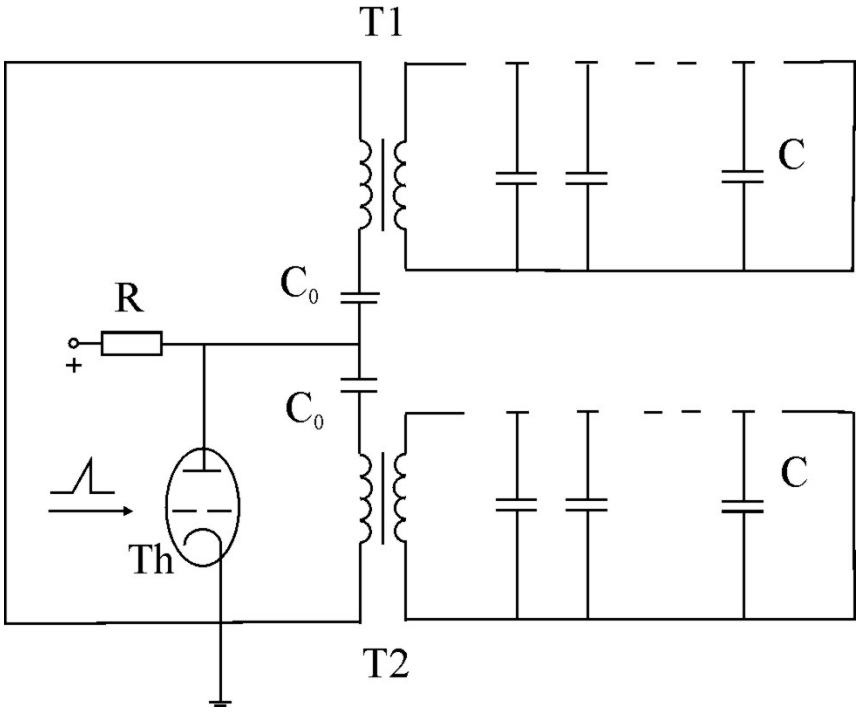

Fig. 1.8. Layout of the electrical circuit developed and designed

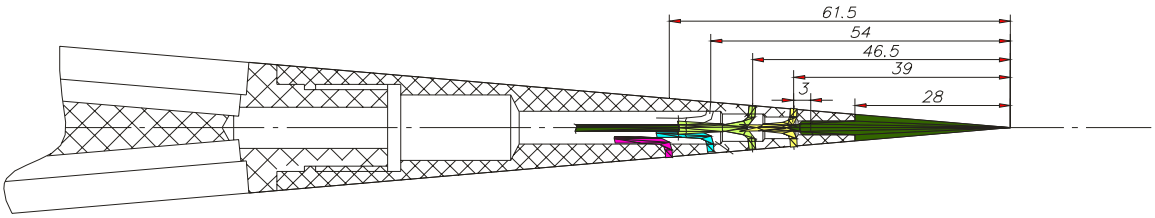

Fig. 1.9. New design of model nose section

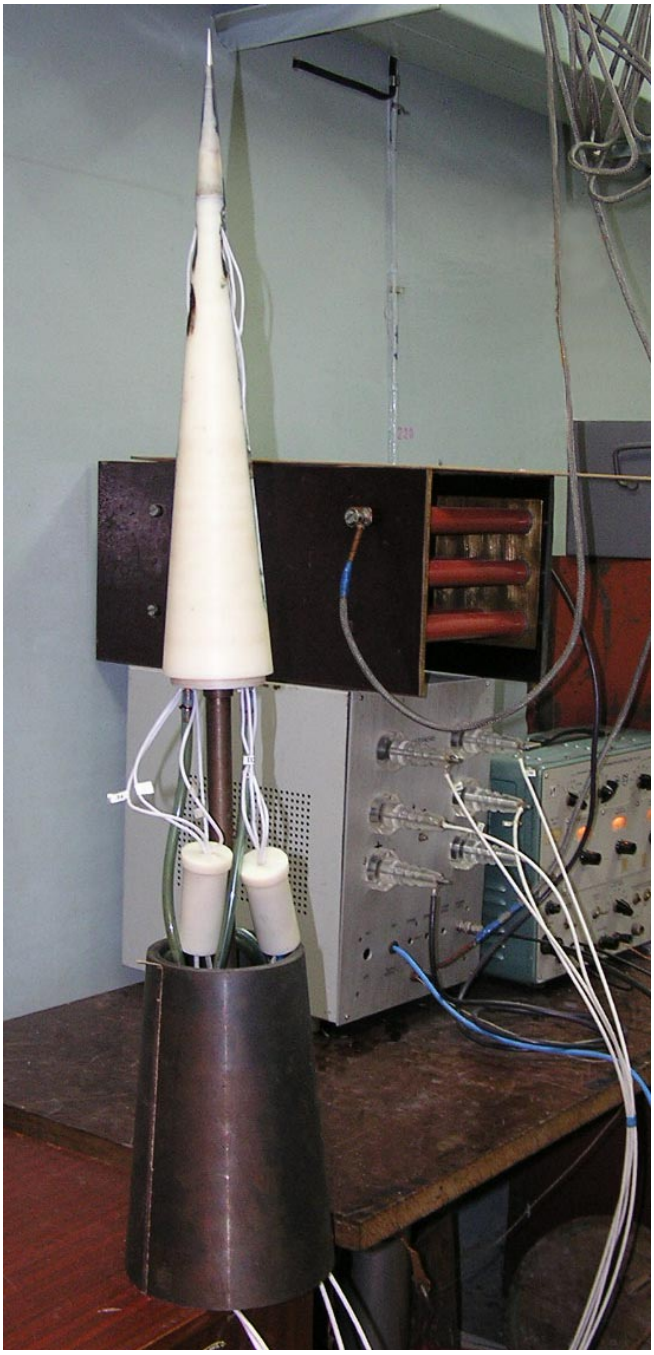

Fig. 1.10. The model assembling

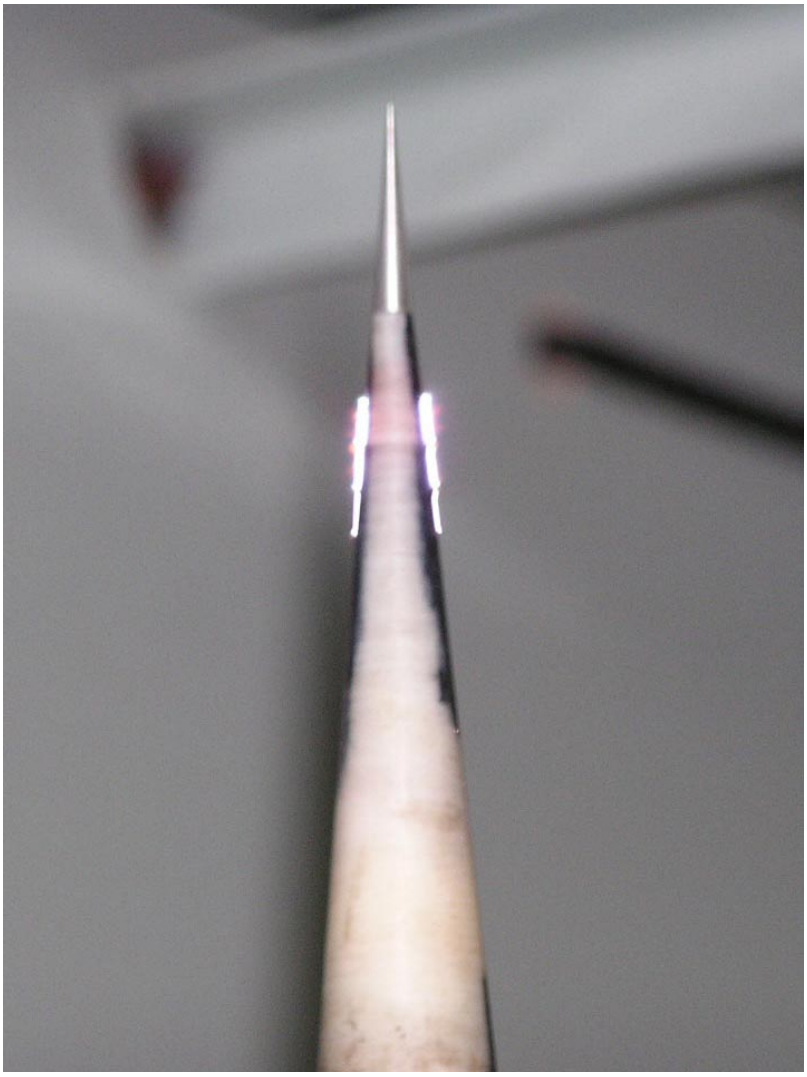

Fig. 1.11. Sparking discharge

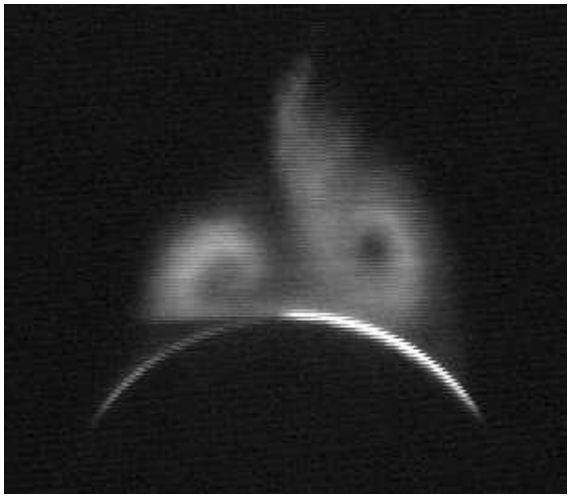

Without discharge

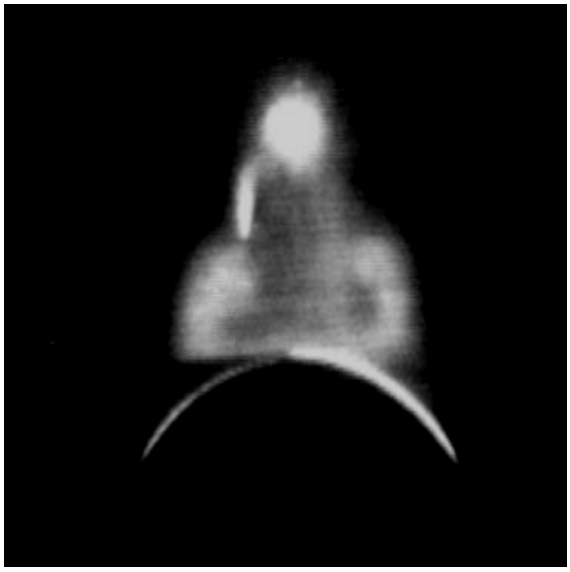

With discharge

Fig. 1.12. AOA=17,5 deg., U_∞=15 m/s
Sharp tip, discharge at the left

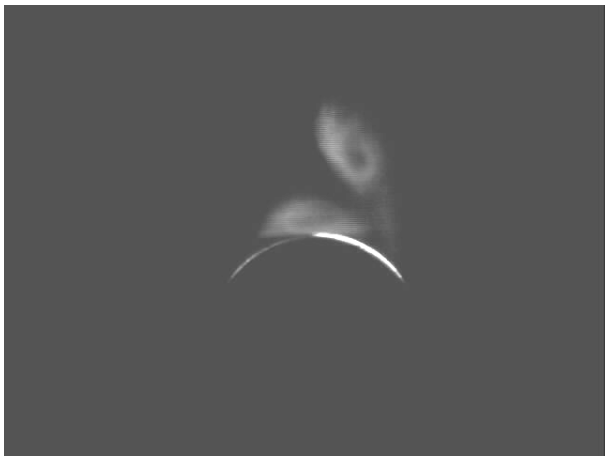

Without discharge

With discharge

Fig. 1.13. AOA=17,5 deg., U_∞=15 m/s
Blunt tip, discharge at the left

Without dischardge

With discharge

Fig. 1.14. AOA=17,5 deg., U_∞=10,7 m/s
Blunt tip, discharge at the left

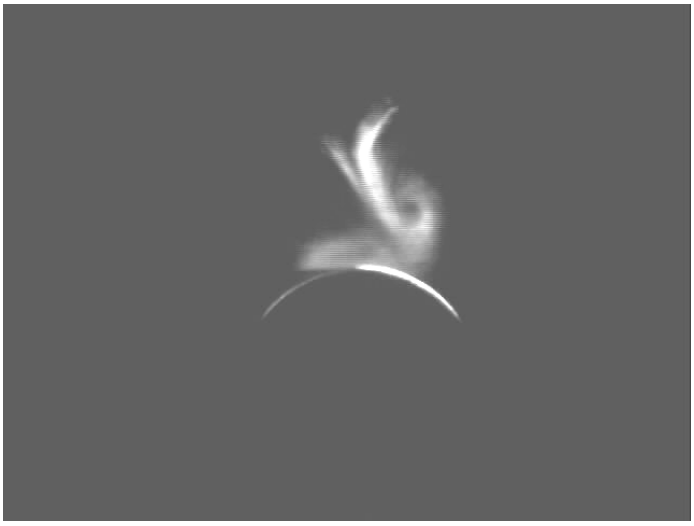

Without discharge

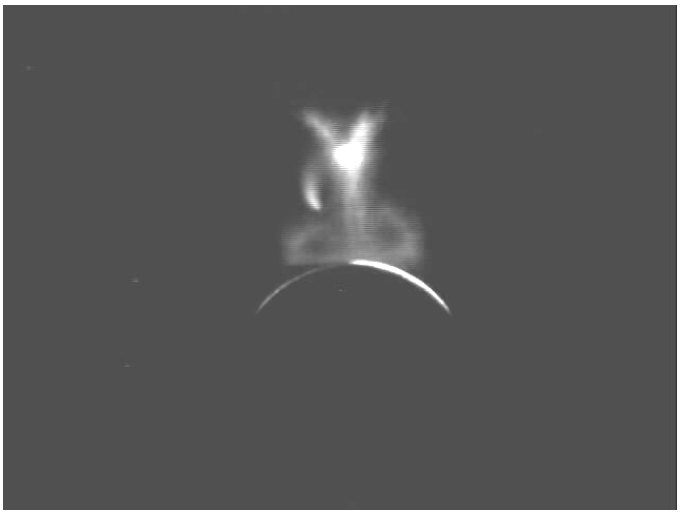

With discharge

Fig. 1.15. AOA=17,5 deg., U_∞=9,2 m/s
Blunt tip, discharge at the left

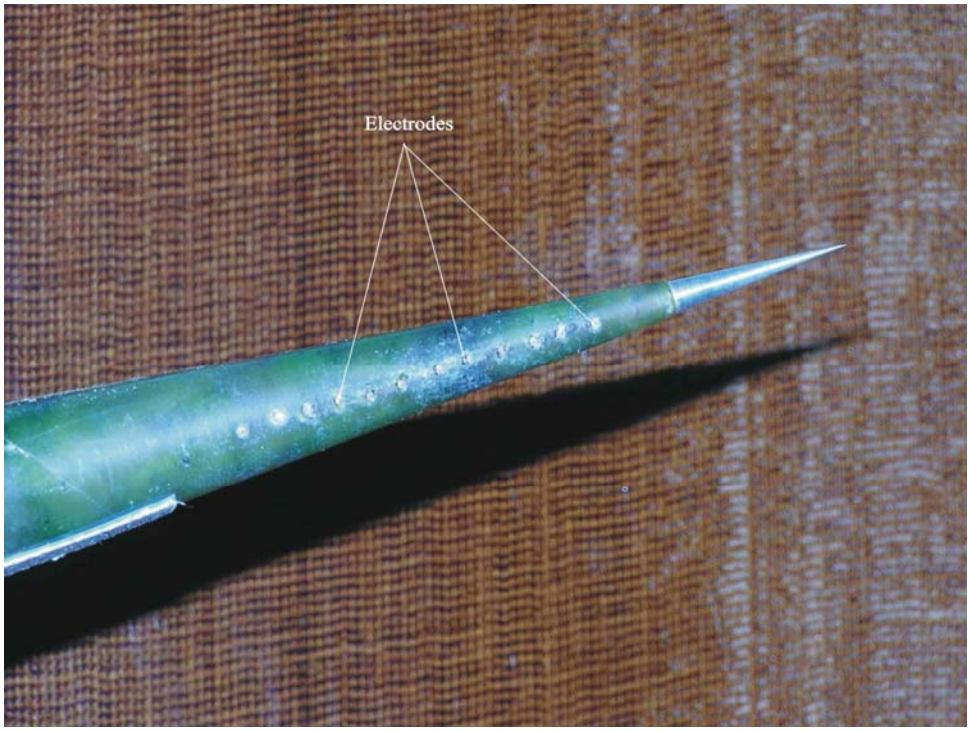

Fig. 1.16. Nose of model made of nephrite

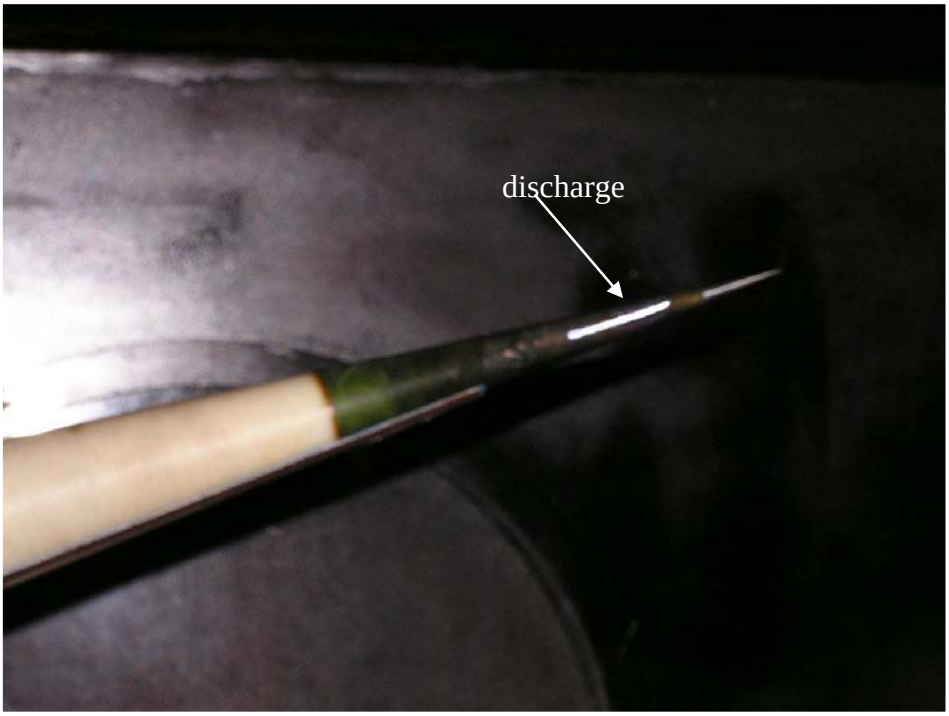

Fig. 1.17. New spark discharge

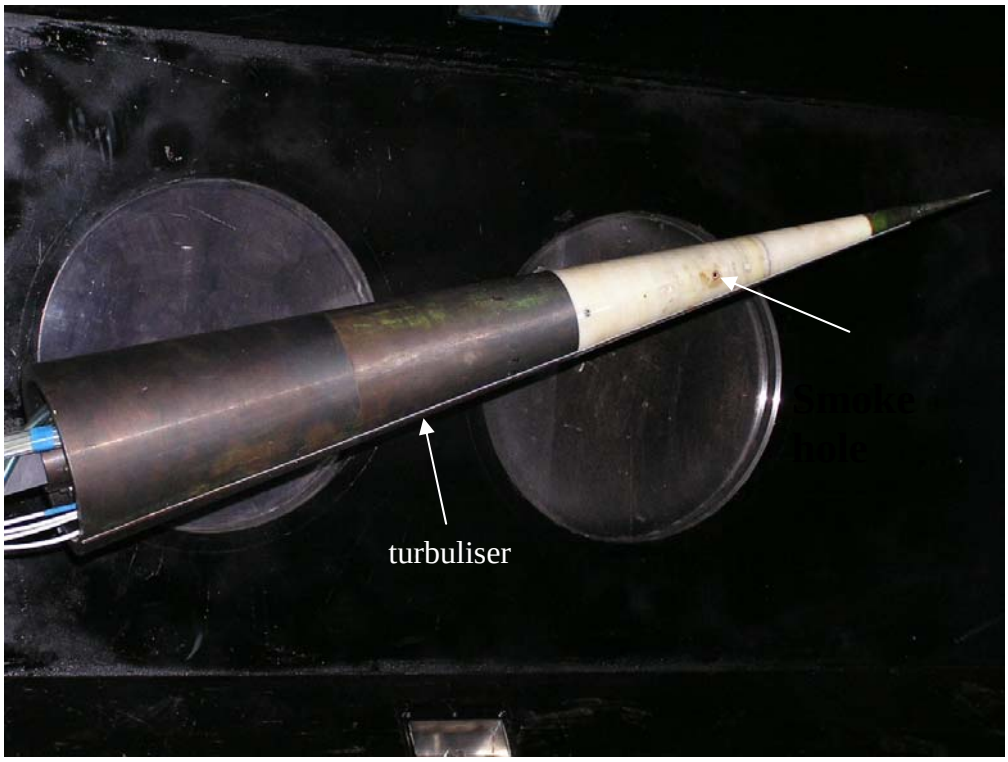

Fig. 1.18. View of turbulisers and smoke hole

Fig. 1.19. Model in the test section of wind tunnel

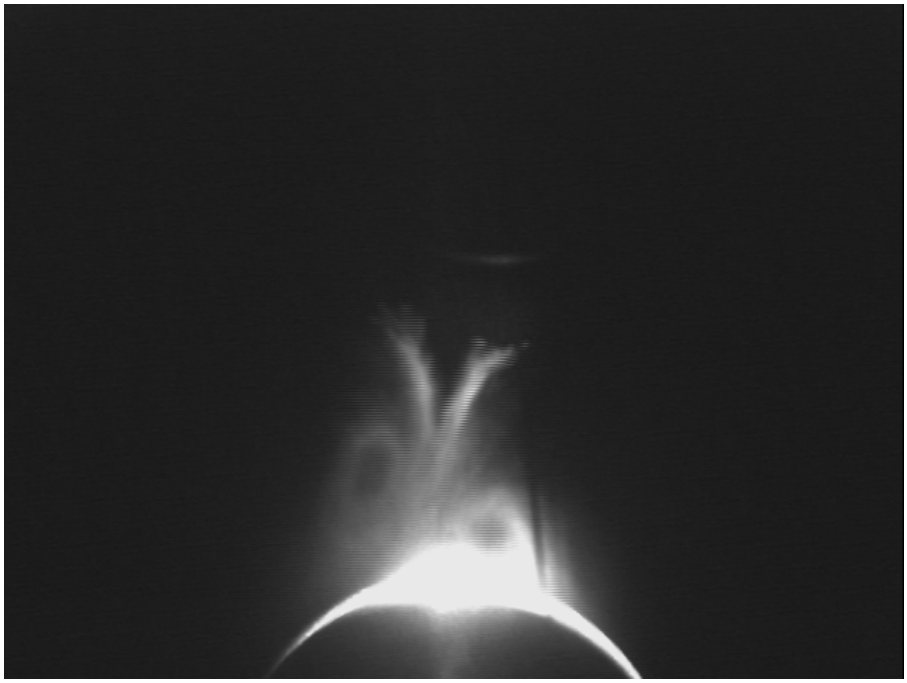

Without discharge

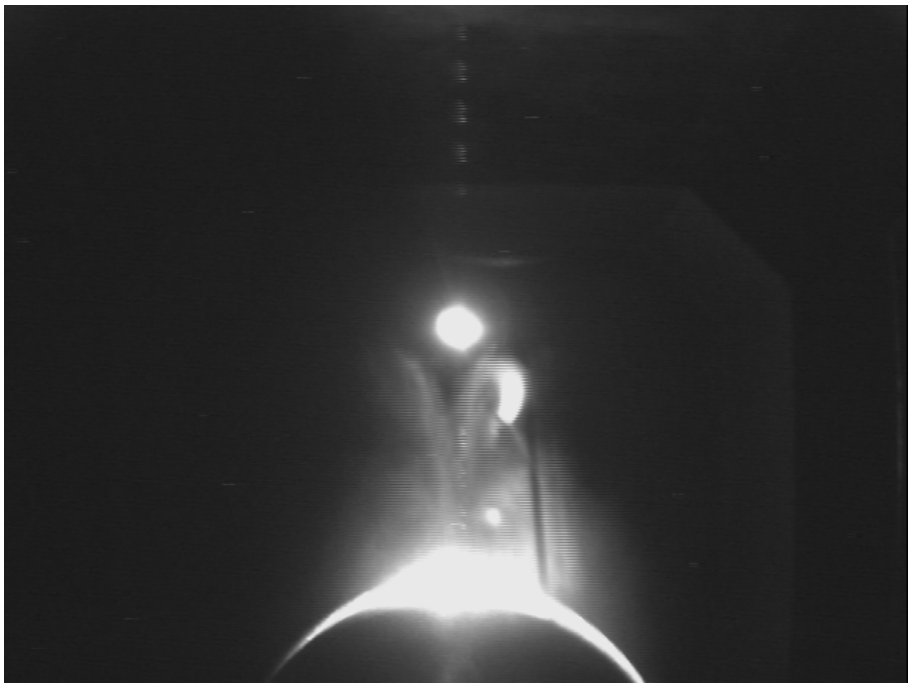

With discharge

Fig. 1.20. Recovery of a symmetry by right discharge;

AOA = 17,5 dg., U_∞ = 10 m/s

Without discharge

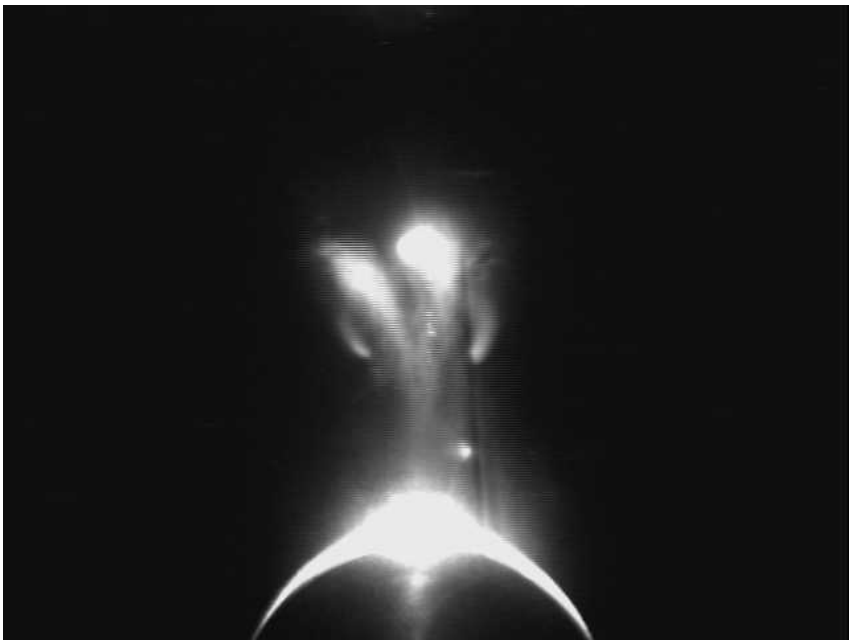

With two discharges

Fig. 1.21. Recovery of a symmetry by two discharges

AOA = 22,5 dgr., U_∞ = 10 m/s

Without discharge

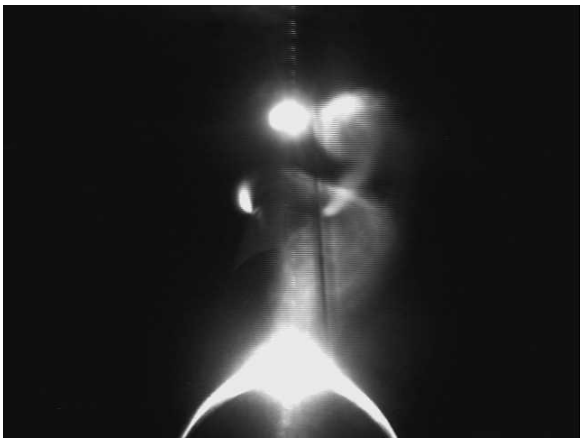

Asymmetrical flow pattern with two discharges

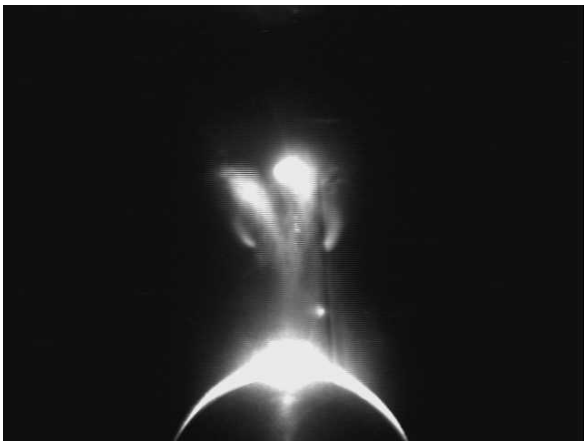

Symmetrical flow pattern with right discharge

Fig. 1.22. Recovery of a symmetry at AOA =30 dgr., U_∞ = 10 m/s

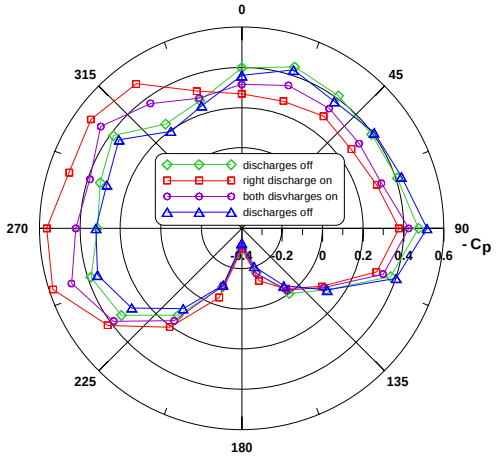

Fig. 1.23. Surface pressure coefficient for right side and both discharges activated, U_∞ = 10 m/s, α = 22.5°

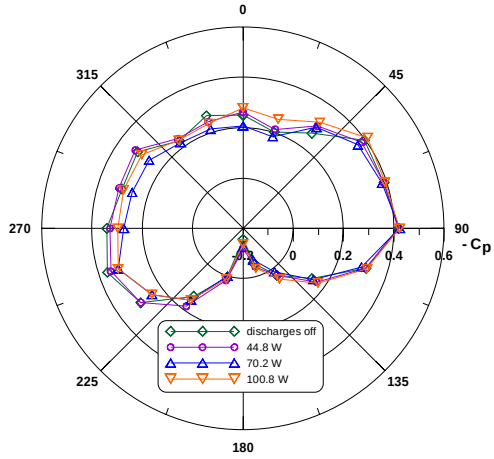

Fig. 1.24. Surface pressure coefficient various left discharge voltages, U_∞ = 10 m/s, α = 17.5°

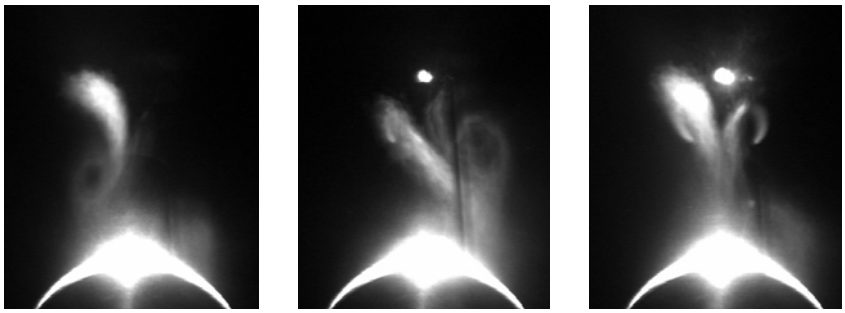

a) **b)** **c)**

Fig. 1.25. Change of vortex configuration with discharge activation; U_∞ = 10 m/s, α = 22.5°, a) both discharges off; b) right discharge on; c) both discharges on.

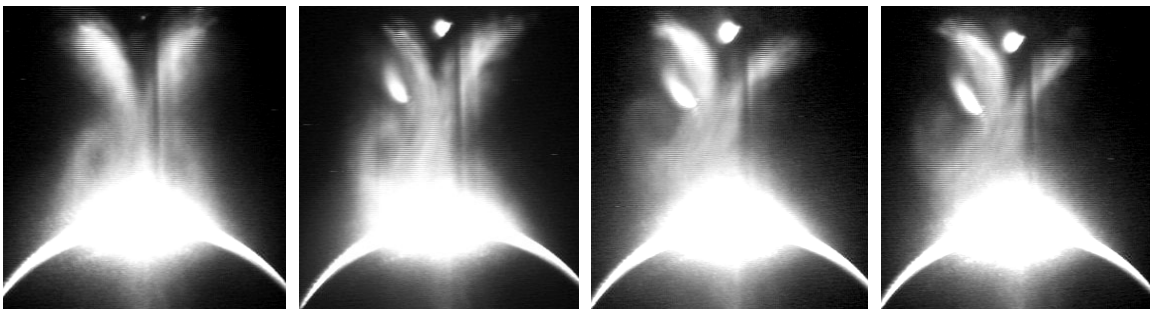

a) **b)** **c)** **d)**

Fig. 1.26. Change of vortex configuration for varying discharge power; U_∞ = 10 m/s, α = 17.5°, a) both discharges off; b) left discharge on, *E*=44.8W; c) left discharge on, *E*=70.2W; d) left discharge on, *E*=100.8W.

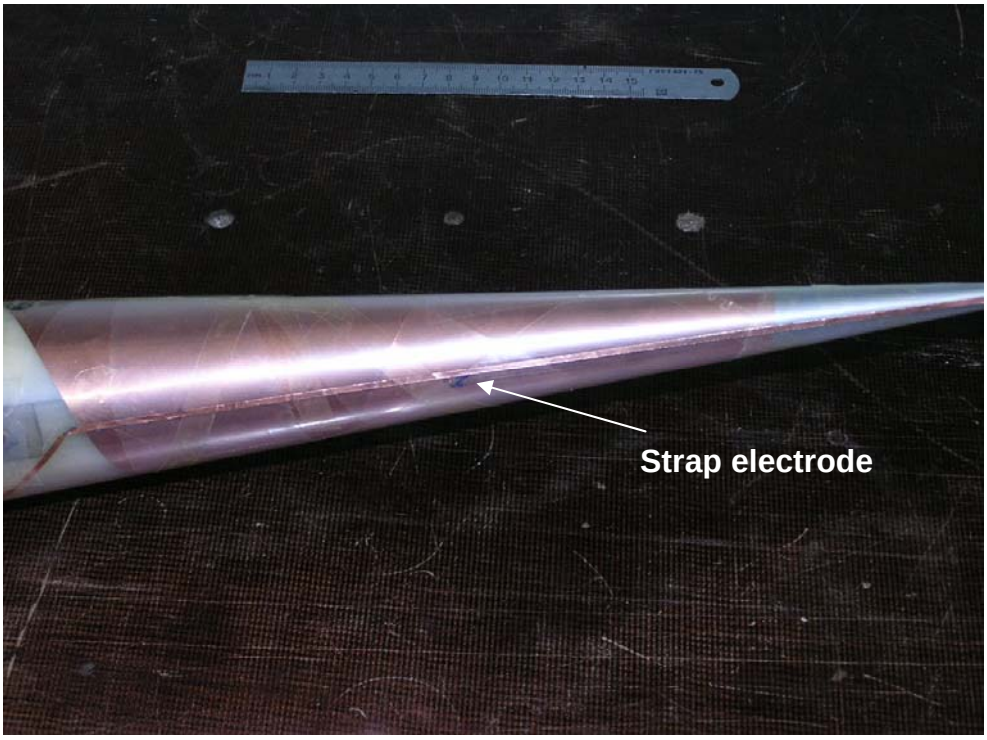

Fig. 1.27. Photo of barrier discharge electrodes

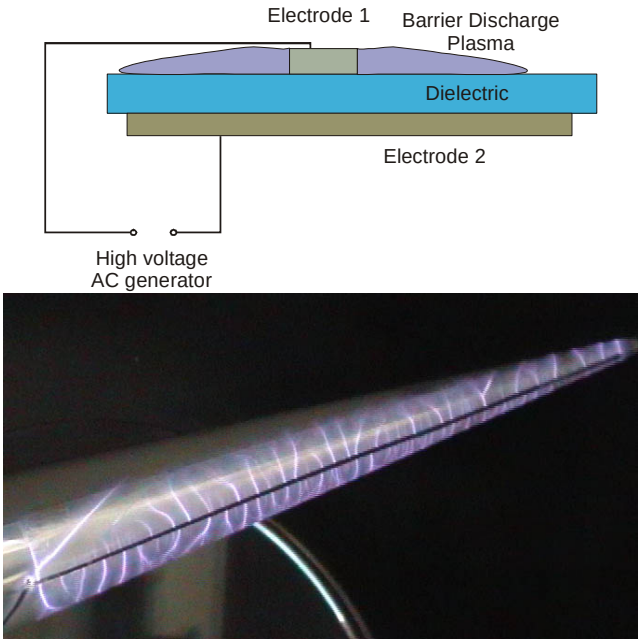

Fig. 1.28. Scheme and photo of symmetric barrier discharge on a strap electrode

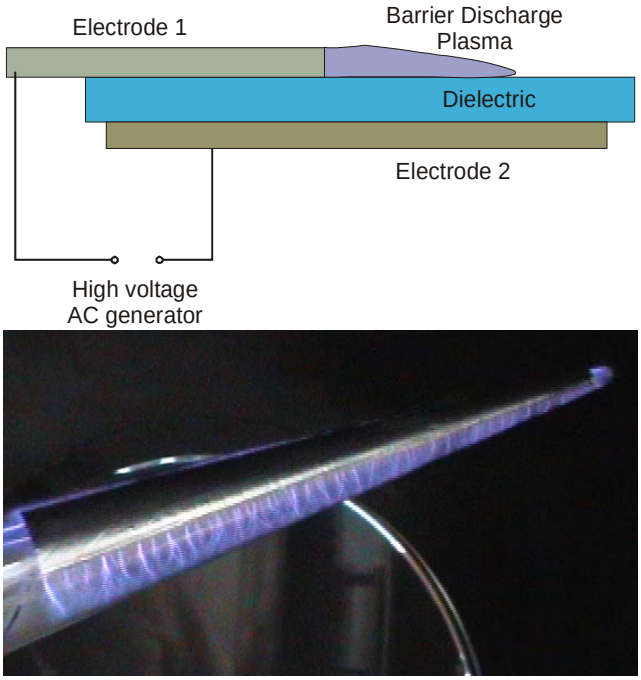

Fig. 1.29. Scheme and photo of asymmetric barrier discharge on a wide upper electrode

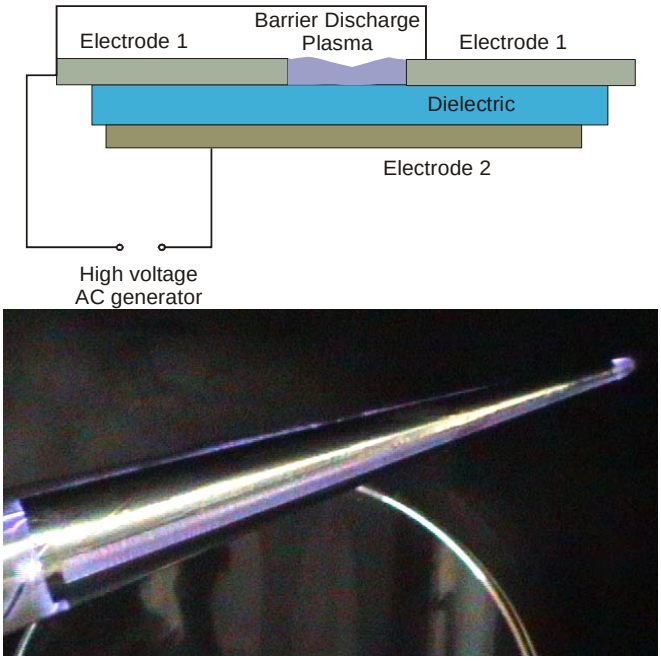

Fig. 1.30. Scheme and photo of barrier discharge in a gap of wide upper electrode

Figures for chapter 2

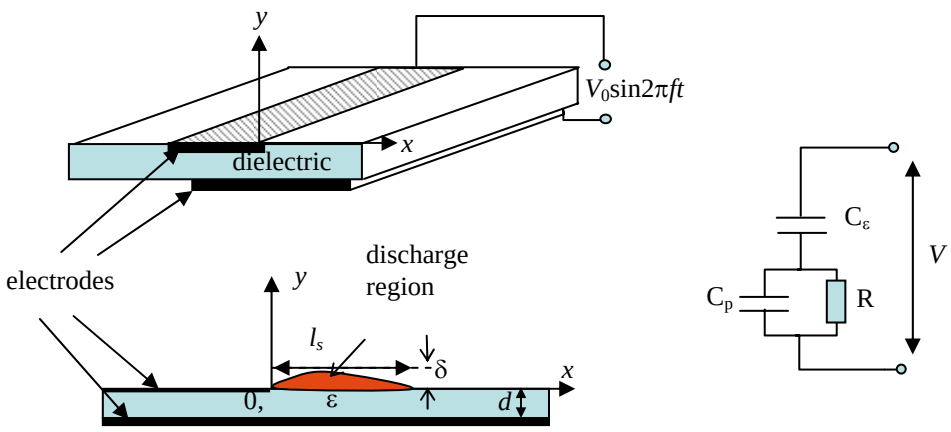

Fig. 2.1. Electrode layout for surface barrier discharge and its equivalent electrical scheme

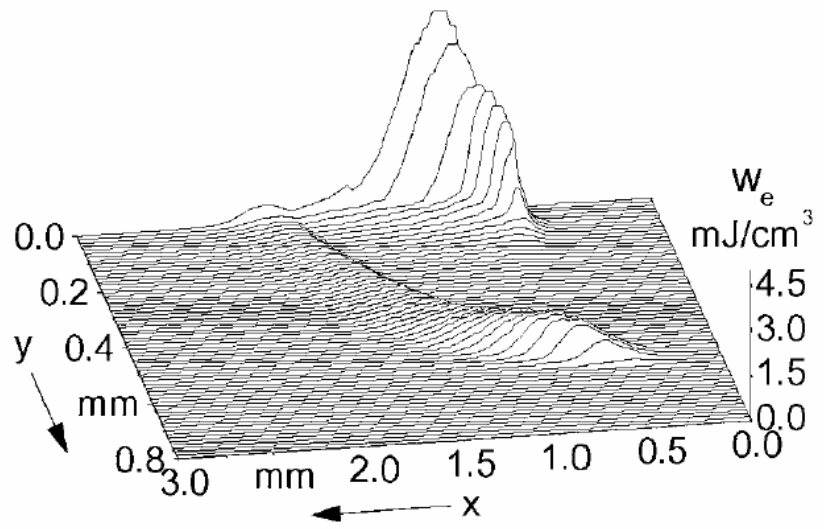

Fig. 2.2. Spatial distribution of specific power deposition in SBD in atmospheric air (V_0 = -11 kV, ε = 5, d = 2 mm) for a time instant of current pulse extinction [24]

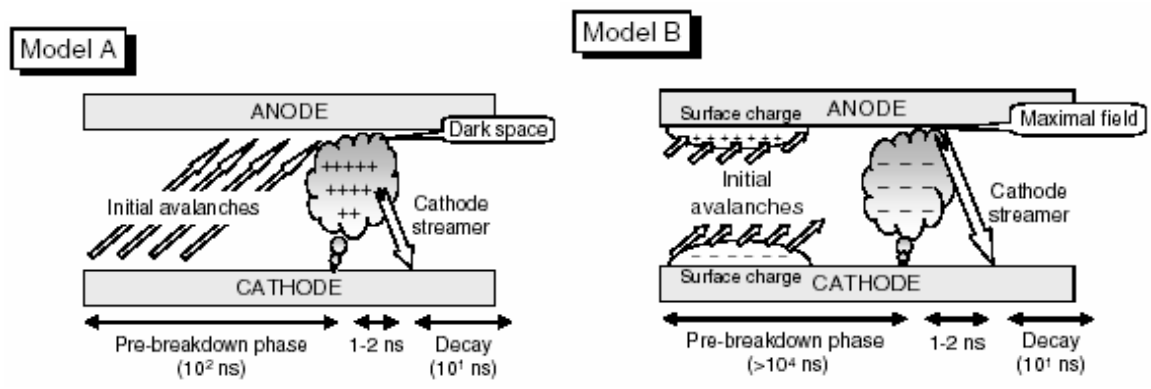

(a) (b)

Fig. 2.3. Schemes of streamer development in barrier discharge [28]; (a) – no initial surface charge on the dielectrics covering the electrodes; (b) – the surface charge from the previous stage of discharge development with opposite electrode polarity is present on the dielectrics covering the electrodes

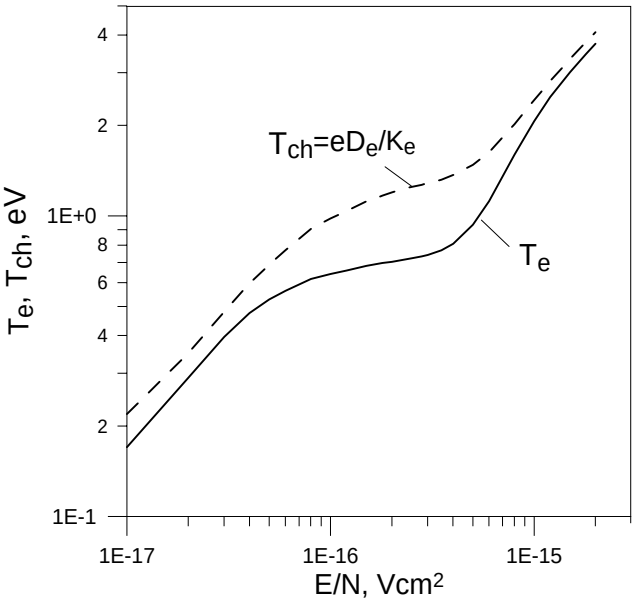

Fig. 2.4. Electron temperature T_e and characteristic electron energy T_{ch} dependence on reduced electric field in air

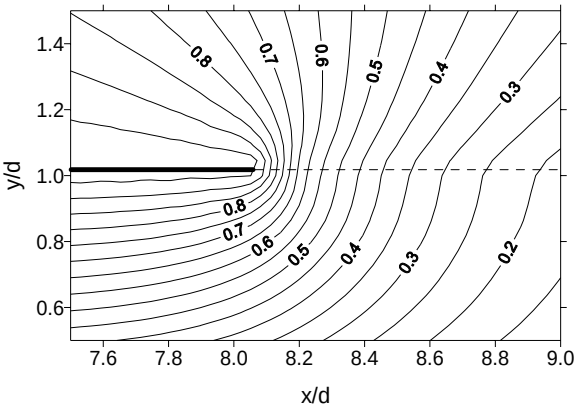

Fig. 2.5. Potential distribution in the vicinity of electrode edge; thick solid line – electrode, dashed line – the dielectric boundary; $V_0 = 1$

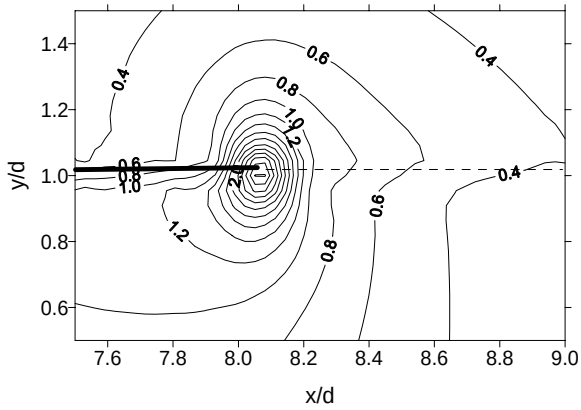

Fig. 2.6. Distribution of electric field absolute value in units of V_0/d; V_0 – potential difference, d – dielectric thickness, $\varepsilon = 10$

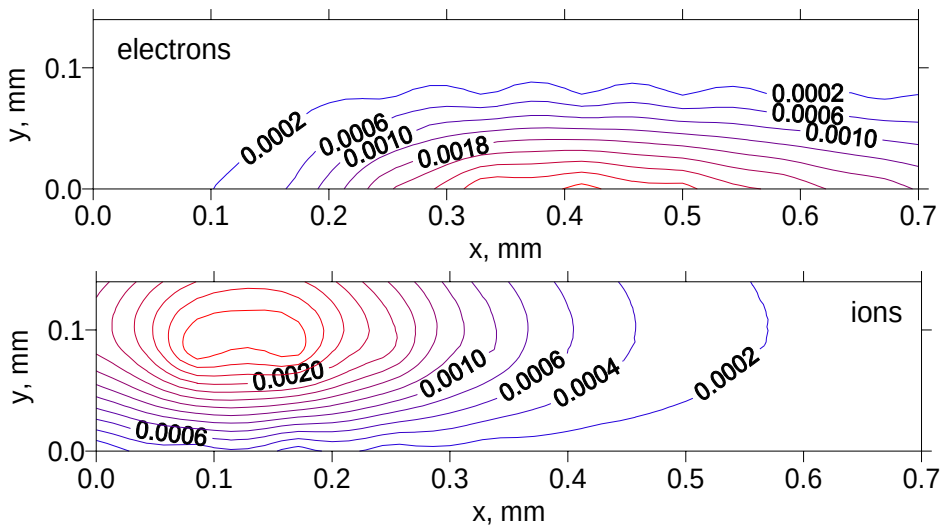

Fig. 2.7. Dimensionless electron $n_e' = \frac{n_e}{n_0}$ (upper picture) and ion $n_i' = \frac{n_i}{n_0}$ (bottom picture) concentration contours for barrier discharge development in atmospheric air at time instant t = 53.4 ns for a model with no air photoionization by discharge region radiation; V = - 4.9 kV, ε = 10, d = 1 mm

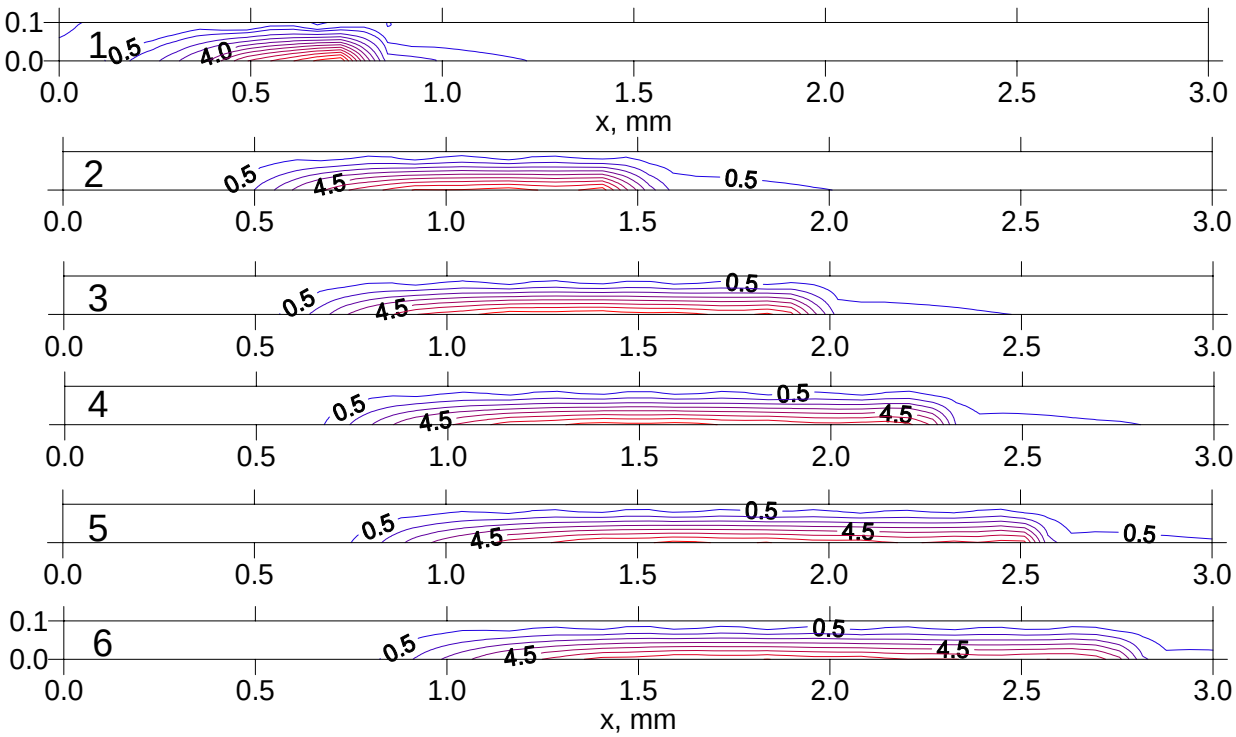

Fig. 2.8. Dimensionless electron concentration $n_e' = \frac{n_e}{n_0}$ contours for barrier discharge development in atmospheric air at time instants t = 8.9 (1), 17.8 (2), 26.7 (3), 35.6 (4), 44.5 (5), and 53.4 ns (6); V = - 4.9 kV, ε = 10, d = 1 mm, β_{ph} = 0.1

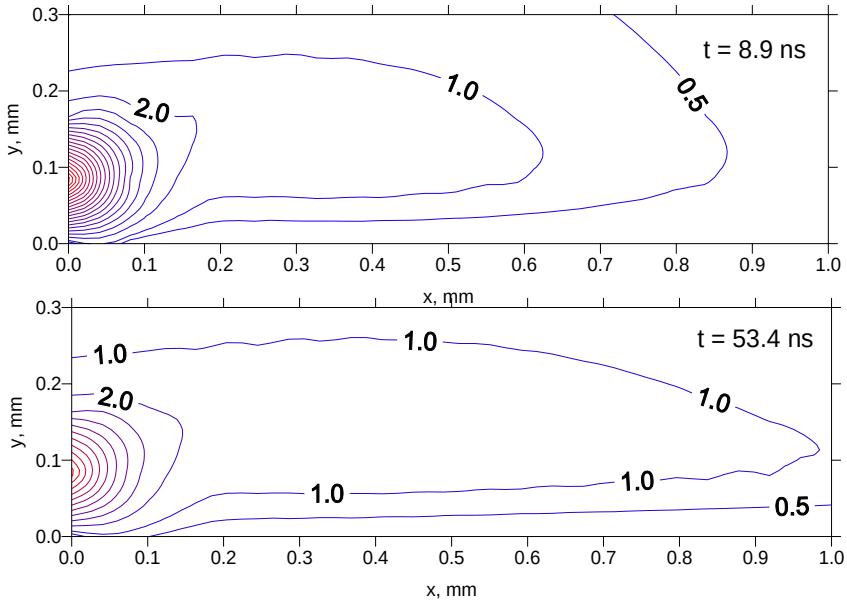

Fig. 2.9. Dimensionless ion $n_i' = \dfrac{n_i}{n_0}$ concentration contours for barrier discharge development in atmospheric air at time instants t = 8.9 and 53.4 ns; V = - 4.9 kV, ε = 10, d = 1 mm, β_{ph} = 0.1

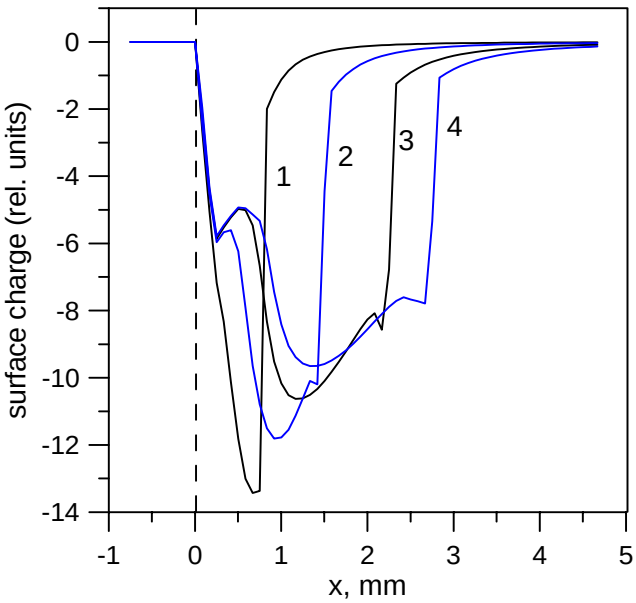

Fig. 2.10. Surface charge density in units of σ_{e0} = 3.5 nC/cm^2 over x-coordinate distribution for time instants t = 8.9 (1), 17.8 (2), 35.6 (3) and 53.4 ns (4); V = - 4.9 kV, ε = 10, d = 1 mm, β_{ph} = 0.1

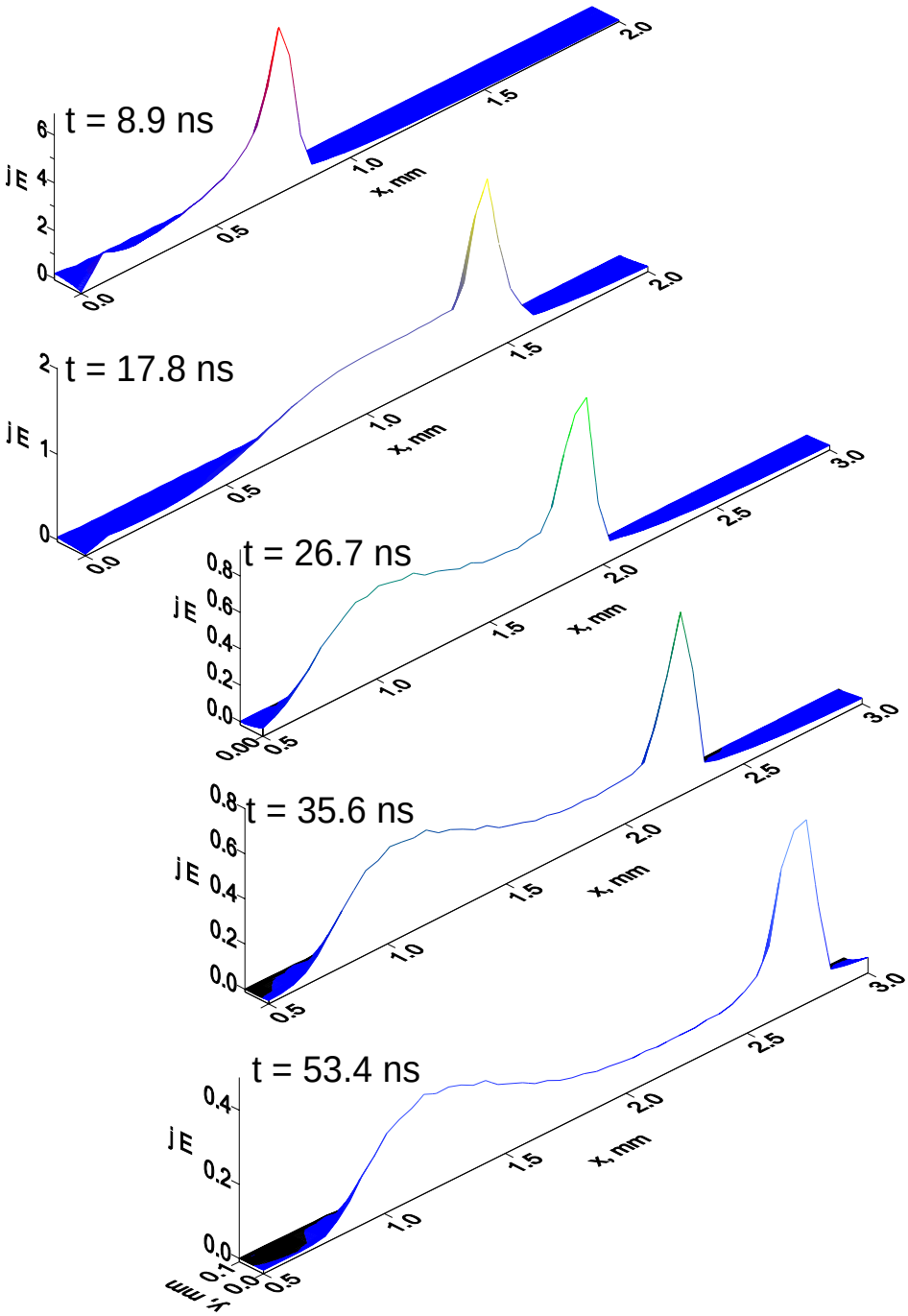

Fig. 2.11. Spatial distribution of power into gas deposition in units of 7.95×10^4 W/cm^3 for different time instants; V = - 4.9 kV, ε = 10, d = 1 mm, β_{ph} = 0.1

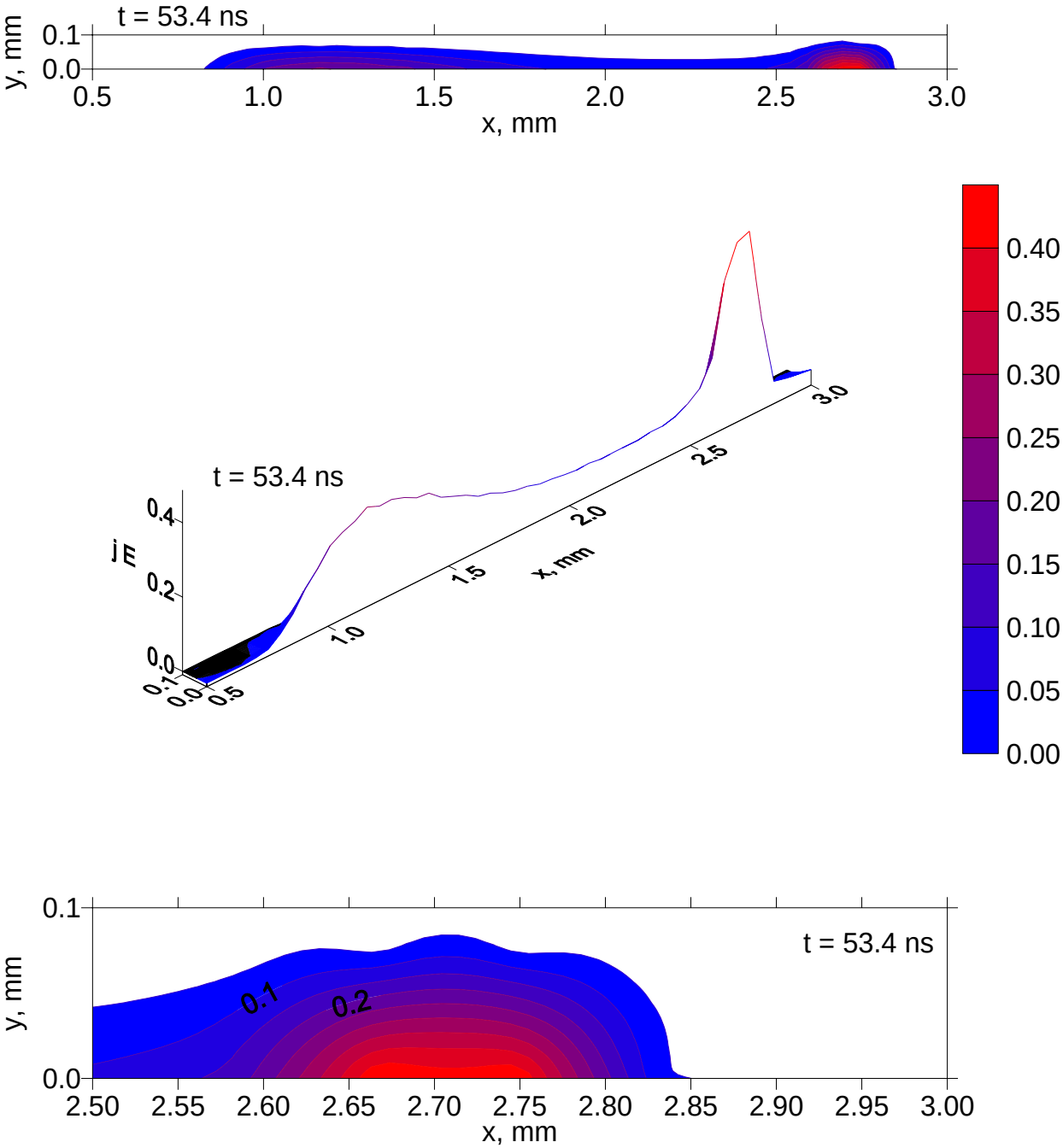

Fig. 2.12. Power into gas deposition in units of 7.95×10^4 W/cm^3 contours for t = 53.4 ns; V = -4.9 kV, ε = 10, d = 1 mm, β_{ph} = 0.1